Journal of Computational Physics 523 (2025) 113634

Contents lists available at ScienceDirect

Journal of Computational Physics

journal homepage: www.elsevier.com/locate/jcp

A double-layer non-hydrostatic model for simulating wave-structure and wave-jet interactions

Yuhang Chen [a,b,c], Yongping Chen [a,b,*], Zhenshan Xu [a,b], Pengzhi Lin [d], Zhihua Xie [c,**]

[a] The National Key Laboratory of Water Disaster Prevention, Hohai University, Nanjing 210098, China
[b] College of Harbor, Coastal and Offshore Engineering, Hohai University, Nanjing 210098, China
[c] School of Engineering, Cardiff University, Queen's Buildings, Cardiff, CF24 3AA, UK
[d] State Key Laboratory of Hydraulics and Mountain River Engineering, Sichuan University, Chengdu, Sichuan 610065, China

A B S T R A C T

Waves are pivotal factors in coastal areas, and effective simulation of wave-related phenomena is crucial. This paper presents the extension of the non-hydrostatic model from single-layer σ transformation to double-layer σ transformation in order to stabilize submerged structures and jet orifices under wave environment. The Lagrangian-Eulerian method is adopted for tracking the free surface in this model. This updated model is validated through comparisons against a series of test cases, including wave structure interaction and horizontal jet under waves. A good agreement between the model results and experimental data is achieved, demonstrating the capability of the developed model to fix the submerged object to resolve wave-structure and wave-jet interactions. Thus, the proposed double-layer σ model can be seen as a useful tool to simulate problems in coastal dynamics.

1. Introduction

Coastal or offshore problems are inherently more complex than those in lakes or channels, primarily due to the presence of dynamic coastal environments such as waves and tidal currents. This complexity often challenges coastal engineers, particularly in the effectiveness of numerical models aimed at addressing these problems. Broadly, these models can be categorized into three distinct types: the potential flow model, the depth-averaged model, and the Navier–Stokes equations (NSE) model.

The potential flow model, grounded in the concept of potential flow, assumes the flow to be irrotational and inviscid (having no viscosity). This model is particularly useful in certain theoretical and practical situations [1–5]. It often enables analytical solutions, thus providing an easier general understanding of flow patterns. However, it falls short in modelling flows that involve shear, vortex, or turbulence, particularly when these flows interact with structures [6]. In contrast, the depth-averaged model, primarily based on the shallow water equation [7–9] or Boussinesq equation [10–14], simplifies the computational process by integrating over the water depth. This reduction in computational dimensions makes the model less time-consuming and faster to execute. However, this model provides a generalized view of fluid flow and might overlook detailed flow characteristics, particularly those that vary in the vertical direction. In contrast to the two previously discussed models, the NSE model solves the full three-dimensional Navier–Stokes equations without simplifications in the vertical direction or restrictions on viscosity, enabling a more accurate representation of three-dimensional flow structures and turbulence in the vertical plane.

The NSE model used in coastal areas mainly undergoes two stages. Early models [15–17] solved the Navier-Stokes equation relied on the hydrostatic pressure assumption, which considers the vertical acceleration of fluid negligible when compared to gravitational

* Corresponding author at Hohai University.
** Corresponding author at Cardiff University.
E-mail addresses: ypchen@hhu.edu.cn (Y. Chen), zxie@cardiff.ac.uk (Z. Xie).

https://doi.org/10.1016/j.jcp.2024.113634
Received 5 March 2024; Received in revised form 12 October 2024; Accepted 25 November 2024

Available online 29 November 2024

force. This assumption was primarily developed for computational efficiency. However, in coastal scenarios, particularly under wave conditions, this assumption does not hold as the vertical acceleration of fluid becomes significant. Consequently, models that solve the full Navier-Stokes equation, which can calculate non-hydrostatic pressure, have gained popularity in coastal engineering. In order to address the computational challenges of capturing air-water interface movements within the NSE, various methods can be effectively utilized. These include the marker-and-cell (MAC) method [18], the volume-of-fluid (VOF) method [19], the level-set method [20], the moment-of-fluid method [21] and so on. These models can capture the free surface accurately and have been applied in many conditions [22–25].

Non-hydrostatic models primarily utilize either Cartesian coordinates [9,26–28] or σ-coordinate [29]. Stelling and Zijlema [26] decomposed the pressure into hydrostatic and non-hydrostatic components and proposed the Keller-box method to replace the staggered grid in the vertical direction, which enables the pressure to be located at the cell faces so that the pressure boundary condition at the free surface can be exactly assigned to zero without any approximation. Their subsequent work [28] in 2008 further developed the model to simulate wave breaking and surf zone dynamics. σ-coordinates, in comparison to Cartesian coordinates, enable precise application of pressure boundary conditions on the free surface [30] and are particularly effective in handling varying water depths. Stansby and Zhou [31] introduced a 2D σ-coordinate model in which the non-hydrostatic pressure is considered. Later, Lin and Li [30] proposed a 3D σ-coordinate model that solves the full Navier-Stokes equations. This model has been validated across various wave propagation scenarios and applied to study wave interactions with vertical piles, both with and without ambient currents. Ma et al. [29] proposed the shock-capturing non-hydrostatic model NHWAVE and can provide good numerical results with relatively fewer vertical layers. Unlike the former non-hydrostatic models, which adopt the vertical integration of the continuity equation plus the appropriate boundary conditions to get the integral form of the kinematic boundary of the free surface, Chen et al. [32] solved the kinematic boundary condition directly using the backward characteristics method with quadratic interpolation polynomial (Lagrangian-Eulerian method) to track the free surface. This model agrees with theoretical and experimental data in various wave environments, including solitary waves or periodic waves and waves interacting with vertical jets. This can be seen as a good supplement to the free surface tracking method in the non-hydrostatic model. Based on that model, Xu et al. [33] expanded the model to include a wave-current interaction module, yielding numerical results that align well with experimental data and effectively simulate flow patterns of vertical jets in wavy-crossflow conditions. In these cases, they assume the vertical jet orifice is near the bottom, where changes in the jet's vertical position are considered acceptable. As a result, they overlook the possibility that the jet's position may move vertically upon changes in water level. However, such an assumption has some limitations, particularly when the vertical jet is positioned higher or when the jet is injected horizontally.

In non-hydrostatic models based on σ-coordinates, structures with vertical faces, whether fixed or floating, tend to move when the water level changes over time. To address this issue, Li and Zhu [34] introduced a double-layer σ transformation model to stabilize objects in the model. Subsequently, Lin [35] developed a more general multi-layer transformation approach to simulate surface wave interactions with various structures, including both floating and emergent types. Ai et al. [22] also adopted a vertical general boundary-fitted coordinate system to fix the obstacles and incorporated the immersed boundary (IB) method to simulate wave-structure interactions. Besides, many studies and methodologies [36–38] provide valuable references. However, to the best of the authors' knowledge, the implementation of such σ coordinates transformation in non-hydrostatic models utilizing the Lagrangian-Eulerian method to track free surface is relatively rare, and its efficiency in simulating wave-related problems remains uncertain.

In this paper, the main novelty is to study the wave-structure interaction problems and the horizontal jet in the wave environment using a non-hydrostatic model in which the Lagrangian-Eulerian method is used to track the free surface. A double-layer σ-coordinate is also developed in the non-hydrostatic model to fix the submerged object or jet orifice. These two aspects distinguish our approach from the non-hydrostatic models discussed above. A series of numerical simulation cases encompassing solitary and regular waves, wave-structure interactions, and jets in wave environments are conducted to verify the model's applicability. The paper is organized as follows: the governing equation and detailed description of the double-layer σ-coordinate are introduced in Section 2. The numerical methods are presented in Section 3. Seven test cases, including solitary wave propagation in constant water depth and over rectangular obstacles, periodic wave propagation in constant water depth and over submerged plates and bars, and flow pattern of the horizontal jet in stagnant and wave environments, are validated in Section 4. Finally, the conclusions are given in Section 5.

2. Mathematical model

2.1. Governing equation and boundary condition

A three-dimensional large eddy simulation model [32,33] is adopted in this study. The model is based on the σ-coordinate and it is governed by the spatially filtered Navier-Stokes equations, which are expressed as follows:

$$\frac{\partial \bar{u}_i}{\partial x_i^*} = 0 \tag{1}$$

$$\frac{\partial \bar{u}_i}{\partial t^*} + \frac{\partial \bar{u}_i \bar{u}_j}{\partial x_j^*} = -\frac{1}{\rho}\frac{\partial \bar{p}}{\partial x_i^*} + g_i + \frac{\partial \tau_{ij}}{\partial x_j^*} - \frac{\partial R_{ij}^{SGS}}{\partial x_j^*} \tag{2}$$

where x_i^* ($i = 1, 2, 3$) are the spatial coordinates in horizontal, transverse and vertical directions, respectively; $\bar{u}_i$ ($i = 1, 2, 3$) are the corresponding velocity components; t^* is the time; ρ is the water density; g_i is the acceleration due to gravity; $\bar{p}$ is the pressure. To simplify the notation, the bars over u_i and p are now removed: u_i stands for $\bar{u}_i$ and p stands for $\bar{p}$. τ_{ij} is the viscous stress and R_{ij}^{SGS} is the sub-grid stress. The viscous stress τ_{ij} can be defined as

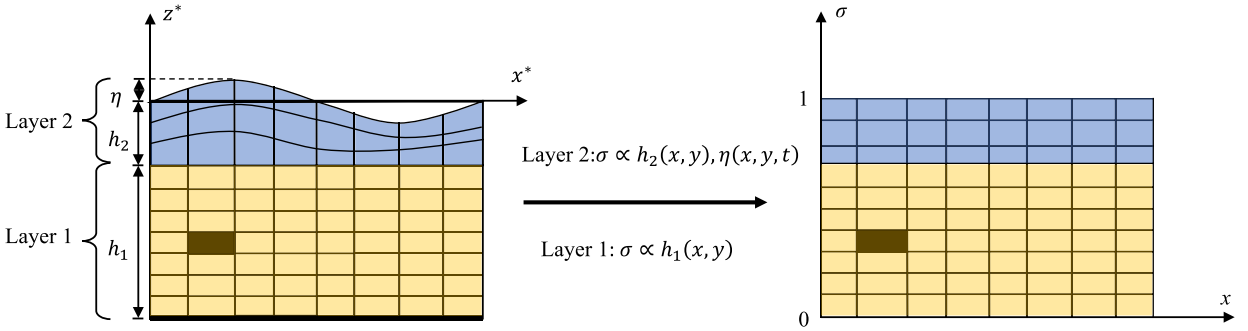

Fig. 1. Sketch of double-layer σ coordinate.

$$\tau_{ij} = 2\nu S_{ij} = \nu\left(\frac{\partial u_i}{\partial {x_j}^*} + \frac{\partial u_j}{\partial {x_i}^*}\right) \tag{3}$$

where ν is the kinematic viscosity. As for the sub-grid stress R_{ij}^{SGS}, it can be composed into a trace-free tensor τ_{ij}^{SGS} and a diagonal tensor $\frac{1}{3}\delta_{ij}R_{kk}$. The diagonal tensor can be absorbed into the pressure term in Equation (2). By applying the standard Smagorinsky model [39], the trace-free tensor can be calculated as:

$$R_{ij}^{SGS} = \tau_{ij}^{SGS} + \frac{1}{3}\delta_{ij}R_{kk} \tag{4}$$

$$\tau_{ij}^{SGS} = -2\nu_t S_{ij} = -\nu_t\left(\frac{\partial u_i}{\partial {x_j}^*} + \frac{\partial u_j}{\partial {x_i}^*}\right) \tag{5}$$

$$\nu_t = \left(C_s\Delta\right)^2\sqrt{2S_{ij}S_{ij}} \tag{6}$$

$$\Delta = \left(\Delta {x_1}^*\Delta {x_2}^*\Delta {x_3}^*\right)^{1/3} \tag{7}$$

where ν_t is the eddy viscosity coefficient; C_s is the Smagorinsky constant and should be calibrated and chosen based on the type of the flow. In this study, the value is set to 0.175; Δ is a representative grid spacing and $\Delta {x_1}^*$, $\Delta {x_2}^*$, $\Delta {x_3}^*$ are the grid sizes in the coordinates of ${x_1}^*$, ${x_2}^*$, ${x_3}^*$, respectively.

The σ coordinate in the vertical coordinate is adopted in this model and σ spans from 0 to 1. The most common used σ-transformation is shown as:

$$\tau = t = t^*, \xi^1 = x_1 = x = x^*, \xi^2 = x_2 = y = y^*, \xi^3 = \sigma = \frac{x_3 + h}{\eta + h} = \frac{z^* + h}{\eta + h} \tag{8}$$

where (x, y, σ, t) are the spatial and time coordinates in the σ coordinate system. It can also be presented as $\left(\xi^1, \xi^2, \xi^3, \tau\right)$; (x^*, y^*, z^*, t^*) are the spatial and time coordinates in the physical domain, respectively. η is the free surface displacement and h is the still water level. To ensure that submerged objects remain stationary and do not move upwards or downwards with changes in water elevation, we implemented the double-layer σ coordinate transformation proposed by Li and Zhu [34] and multi-layer σ transformation proposed by Lin and Li [30] into the model. The sketch of the double-layer σ transformation is shown in Fig. 1.

The double-layer σ coordinate transformation and their corresponding spatial and temporal derivatives are presented as follows:

$$D(x,y,t) = h(x,y) + \eta(x,y,t) = h_1(x,y) + h_2(x,y) + \eta(x,y,t) \tag{9}$$

$$\alpha = \frac{h_1(x,y)}{h_1(x,y) + h_2(x,y)}, \beta = \frac{h_2(x,y)}{h_1(x,y) + h_2(x,y)} \tag{10}$$

$$\sigma = \begin{cases} \alpha + \beta\frac{h_2(x,y)+z^*(x,y)}{h_2(x,y)+\eta(x,y,t)} & , -h_2(x,y) \le z^* \le \eta(x,y,t) \\ \alpha\frac{h_1(x,y)+h_2(x,y)+z^*(x,y)}{h_1(x,y)} & , -h_1(x,y) - h_2(x,y) \le z^* < -h_2(x,y) \end{cases} \tag{11}$$

$$\frac{\partial\sigma}{\partial t^*} = \begin{cases} -\frac{\sigma-\alpha}{D(x,y,t)-h_1(x,y)}\frac{\partial\left(D(x,y,t)-h_1(x,y)\right)}{\partial t} & , \alpha \le \sigma \le 1 \\ 0 & , 0 \le \sigma < \alpha \end{cases} \tag{12}$$

$$\frac{\partial\sigma}{\partial x^*} = \begin{cases} -\frac{\sigma-\alpha}{D(x,y,t)-h_1(x,y)}\frac{\partial\left(D(x,y,t)-h_1(x,y)\right)}{\partial x} + \frac{\beta}{D(x,y,t)-h_1(x,y)}\frac{\partial\left(h_2(x,y)\right)}{\partial x} & , \alpha \le \sigma \le 1 \\ -\frac{\sigma-\alpha}{h_1(x,y)}\frac{\partial\left(h_1(x,y)\right)}{\partial x} + \frac{\alpha}{h_1(x,y)}\frac{\partial\left(h_2(x,y)\right)}{\partial x} & , 0 \le \sigma < \alpha \end{cases} \tag{13}$$

$$\frac{\partial \sigma}{\partial y^*} = \begin{cases} -\frac{\sigma-\alpha}{D(x,y,t)-h_1(x,y)}\frac{\partial\left(D(x,y,t)-h_1(x,y)\right)}{\partial y} + \frac{\beta}{D(x,y,t)-h_1(x,y)}\frac{\partial\left(h_2(x,y)\right)}{\partial y} & , \alpha \le \sigma \le 1 \\ -\frac{\sigma-\alpha}{h_1(x,y)}\frac{\partial\left(h_1(x,y)\right)}{\partial y} + \frac{\alpha}{h_1(x,y)}\frac{\partial\left(h_2(x,y)\right)}{\partial y} & , 0 \le \sigma < \alpha \end{cases} \tag{14}$$

$$\frac{\partial \sigma}{\partial z^*} = \begin{cases} \frac{\beta}{D(x,y,t)-h_1(x,y)} & , \alpha \le \sigma \le 1 \\ \frac{\alpha}{h_1(x,y)} & , 0 \le \sigma < \alpha \end{cases} \tag{15}$$

where $D(x,y,t)$ is the total depth; $h_1(x,y)$ and $h_2(x,y)$ are bottom layer depth and top layer depth, respectively; α and β are weighting coefficients for the two layers and they can be chosen arbitrarily. Additionally, it becomes evident that when α is sufficiently small, the double-layer model simplifies to a single-layer model, a claim that will be substantiated in Section 4. After the σ transformation, the spatially filtered Navier-Stokes equations can be expressed as

$$\frac{\partial u_i}{\partial \xi^k}\frac{\partial \xi^k}{\partial x_i^*} = 0 \tag{16}$$

$$\frac{\partial u_i}{\partial \tau} + \frac{\partial u_i}{\partial \xi^k}\frac{\partial \xi^k}{\partial t^*} + u_j\frac{\partial u_i}{\partial \xi^k}\frac{\partial \xi^k}{\partial x_j^*} = -\frac{1}{\rho}\frac{\partial p}{\partial \xi^k}\frac{\partial \xi^k}{\partial x_i^*} + g_i + \frac{\partial \tau_{ij}}{\partial \xi^k}\frac{\partial \xi^k}{\partial x_j^*} - \frac{\partial R_{ij}^{SGS}}{\partial \xi^k}\frac{\partial \xi^k}{\partial x_j^*} \tag{17}$$

2.2. Boundary condition

As for the inflow condition, the velocity and free surface displacement are given by analytical solutions. For progressive waves, a ramp function is applied to the inflow boundary function to mitigate initial numerical oscillations, and it is expressed as follows:

$$\phi_R = \phi \tanh\left(\frac{t}{2\pi T}\right) \tag{18}$$

where ϕ represents the analytical solution for wave elevation or water particle velocity; T denotes the wave period, and ϕ_R is the resulting boundary condition. Regarding the pressure boundary condition, a simpler assumption can be made that vertical accelerations of fluids are small and can be neglected [30]. The final pressure boundary condition can be expressed as follows:

$$\frac{\partial p}{\partial x} + \frac{\partial p}{\partial \sigma}\frac{\partial \sigma}{\partial x^*} = -\rho g_3\frac{\partial \eta}{\partial x}, \frac{\partial p}{\partial y} + \frac{\partial p}{\partial \sigma}\frac{\partial \sigma}{\partial y^*} = -\rho g_3\frac{\partial \eta}{\partial y} \tag{19}$$

A zero-gradient condition is applied in the normal direction at the front, back wall boundaries and obstacle boundary. For the bottom boundary, we employ a free-slip condition to estimate velocity gradients at the first interior node, which will be subsequently used in the advection calculation. The log-law wall function is also utilized to compute wall shear stress during the diffusion step. This approach has yielded reasonable results with relatively coarse meshes [30,40]. At the outflow boundary, the radiation condition is adopted. At the moving free surface η, the kinematic boundary condition is

$$\frac{\partial \eta}{\partial t^*} + u_1\frac{\partial \eta}{\partial x^*} + u_2\frac{\partial \eta}{\partial y^*} - u_3 = 0 \tag{20}$$

When the wave is present, a damping zone is used to reduce the wave reflection. The damping method utilized in this study is slightly modified from the method proposed by Park et al. [41]. It can be expressed as follows:

$$\varphi_R = \varphi + \Delta t \cdot \gamma \cdot \sigma \cdot \left(\frac{x - x_s}{x_e - x_s}\right)^2 \cdot \left(\varphi - \varphi_0\right) \tag{21}$$

where φ is the variable to be solved (i.e., u_i and η); φ_R is the resulting variable after the numerical damping; γ is the empirical parameter and equals -1.0 in this study. The subscripts s and e denote the start and end points of the damping zone in the x direction.

The jet outlet velocity boundary is generated by the SEM (Synthetic-Eddy-Method) [42]. The velocity field on the inflow boundary plane for LES is decomposed to a time-averaged and a fluctuating component. The fluctuating component of the velocity field at a node on the LES inflow plane is given by

$$u_i(x,t) = \bar{u}_i(x) + a_{ij}u_j'(x,t) = \bar{u}_i(x) + a_{ij}\frac{\delta}{\sqrt{N}}\sum_{k=1}^{N}\varepsilon_j^k f_\sigma(x - x^k(t)) \tag{22}$$

$$a_{ij} = \begin{pmatrix} \sqrt{R_{11}} & 0 & 0 \\ R_{21}/a_{11} & \sqrt{R_{22} - a_{21}^2} & 0 \\ R_{31}/a_{11} & \left(R_{32} - a_{21}a_{31}\right)/a_{22} & \sqrt{R_{33} - a_{31}^2 - a_{32}^2} \end{pmatrix} \tag{23}$$

$$f_\sigma(x - x^k(t)) = \sqrt{\frac{V_B}{\sigma_x\sigma_y\sigma_z}} \cdot f\left(\frac{x - x^k(t)}{\sigma_x}\right) \cdot f\left(\frac{y - y^k(t)}{\sigma_y}\right) \cdot f\left(\frac{z - z^k(t)}{\sigma_z}\right) \tag{24}$$

Where $\bar{u}_i(x)$ is the time-averaged component of the velocity; a_{ij} is the Cholesky decomposition of the Reynolds stress tensor R_{ij}; u_j' is the fluctuating velocity at j direction; δ is a parameter to enlarge the turbulence properties, and it can be set as 1.0; N is the number of eddies and is set as 35 in this study; ϵ_j^k is the randomly drawn from -1 or +1; x^k is the location of eddy; σ_i is the length scale of eddy and is set as 0.004 m; V_B is the volume of the eddy box and equals the area of jet multiples σ_i. $f(\zeta)$ is the shape function and it can be written as [43]:

$$f(\zeta) = \begin{cases} \sqrt{1.5}(1-|\zeta|) & |\zeta| \le 1 \\ 0 & |\zeta| > 1 \end{cases} \tag{25}$$

The distribution of time-averaged velocity assigned to each grid point can be written as Equation (26) [44]. The relation between the velocity at the center of the jet orifice and time-averaged velocity at the cross-section can also be written as Equation (27) using fitting method [45]. The fluctuation velocity and Reynolds stress distribution of the jet are aligned with the DNS results performed by Wu and Moin [46].

$$\frac{\bar{u}}{u_c} = \left(1 - \frac{r}{R}\right)^{\frac{1}{n}} \tag{26}$$

$$\frac{u_c}{u_0} = \frac{0.744}{Re^{0.113}} + 1 \tag{27}$$

where u_c is the velocity at the center of the jet orifice; R is the radius of the nozzle; n is a constant and is set as 6.6 in this study; u_0 is the time-averaged velocity at the cross-section; Re is the Reynolds number which equals $\frac{u_0 \cdot 2R}{\nu}$.

3. Numerical method

3.1. Numerical schemes for Navier-Stokes equations

The numerical solution procedure for this non-hydrostatic model is primarily divided into two stages. In the first stage, the operator splitting method [17,47,48] is employed to solve the Navier-Stokes equations, obtaining the velocity and pressure at various time steps. Subsequently, the Lagrangian-Eulerian method updates the water surface following the velocity computed in the preceding stage. The operator splitting method involves a three-step process at each time step for the momentum equations: advection, diffusion, and pressure propagation. For simplicity, we only focus on the numerical discretization in the x direction. The same approach is applicable to the y and z directions, respectively.

For the advection step,

$$\frac{(u_1)_{i,j,k}^{n+1/3} - (u_1)_{i,j,k}^{n}}{\Delta\tau} = -\left(\frac{\partial u_i}{\partial \xi^k}\frac{\partial \xi^k}{\partial t^*} + u_j\frac{\partial u_i}{\partial \xi^k}\frac{\partial \xi^k}{\partial x_j^*}\right)^n = -\left(u_1\frac{\partial u_1}{\partial x} + u_2\frac{\partial u_1}{\partial y} + \omega\frac{\partial u_1}{\partial \sigma}\right)_{i,j,k}^n \tag{28}$$

$$\omega = \frac{\partial \sigma}{\partial t^*} + u_1\frac{\partial \sigma}{\partial x^*} + u_2\frac{\partial \sigma}{\partial y^*} + u_3\frac{\partial \sigma}{\partial z^*} \tag{29}$$

Equation (28) can be split into the following three sub-steps:

$$\begin{aligned} \frac{(u_1)_{i,j,k}^{n+1/9} - (u_1)_{i,j,k}^{n}}{\Delta\tau} &= -\left(u_1\frac{\partial u_1}{\partial x}\right)_{i,j,k}^{n} \\ \frac{(u_1)_{i,j,k}^{n+2/9} - (u_1)_{i,j,k}^{n+1/9}}{\Delta\tau} &= -\left(u_2\frac{\partial u_1}{\partial y}\right)_{i,j,k}^{n+1/9} \\ \frac{(u_1)_{i,j,k}^{n+3/9} - (u_1)_{i,j,k}^{n+2/9}}{\Delta\tau} &= -\left(\omega\frac{\partial u_1}{\partial \sigma}\right)_{i,j,k}^{n+2/9} \end{aligned} \tag{30}$$

The combination of the quadratic backward characteristic method [49] and the Lax-Wendroff method is used to solve the flow advection. In order to employ the quadratic backward characteristics method, the advection distance Δx_a is defined as $\Delta x_a = (u_1)_{i,j,k}^n \Delta\tau$, equation can be solved as

$$\begin{aligned} \left[(u_1)_{i,j,k}^{n+1/9}\right]_{QC} = &\frac{(\Delta x_{i-1} - \Delta x_a)(-\Delta x_a)}{\Delta x_{i-2}(\Delta x_{i-2} + \Delta x_{i-1})}(u_1)_{i-2,j,k}^n + \frac{(\Delta x_{l-2} + \Delta x_{i-1} - \Delta x_a)(-\Delta x_a)}{(\Delta x_{i-2})(-\Delta x_{i-1})}(u_1)_{i-1,j,k}^n \\ &+ \frac{(\Delta x_{i-2} + \Delta x_{i-1} - \Delta x_a)(\Delta x_{i-1} - \Delta x_a)}{(\Delta x_{i-2} + \Delta x_{i-1})\Delta x_{i-1}}(u_1)_{i,j,k}^n \end{aligned} \tag{31}$$

Equation (30) can be discretized by the Lax-Wendroff method as:

$$\left[(u_1)_{i,j,k}^{n+1/9}\right]_{LW} = \frac{\Delta x_a\left(\Delta x_i + \Delta x_a\right)}{\Delta x_{i-1}\left(\Delta x_{i-1} + \Delta x_i\right)}(u_1)_{i-1,j,k}^{n} + \frac{\left(\Delta x_{i-1} - \Delta x_a\right)\left(-\Delta x_i - \Delta x_a\right)}{\Delta x_{i-1}\left(-\Delta x_i\right)}(u_1)_{i,j,k}^{n} + \frac{\left(\Delta x_{i-1} - \Delta x_a\right)\left(-\Delta x_a\right)}{\left(\Delta x_{i-1} + \Delta x_i\right)\Delta x_i}(u_1)_{i+1,j,k}^{n} \tag{32}$$

The average value derived from the two aforementioned methods is utilized to ensure consistent and precise numerical results [30]:

$$(u_1)_{i,j,k}^{n+1/9} = \frac{\left[(u_1)_{i,j,k}^{n+1/9}\right]_{QC} + \left[(u_1)_{i,j,k}^{n+1/9}\right]_{LW}}{2} \tag{33}$$

For the diffusion step,

$$\frac{(u_1)_{i,j,k}^{n+2/3} - (u_1)_{i,j,k}^{n+1/3}}{\Delta\tau} = \left(\frac{\partial\tau_{ij}}{\partial\xi^k}\frac{\partial\xi^k}{\partial x_j^*} - \frac{\partial R_{ij}^{SGS}}{\partial\xi^k}\frac{\partial\xi^k}{\partial x_j^*}\right)^{n+1/3} \tag{34}$$

The stress term can be calculated according to Equation (3) and Equation (5). The central difference is used to discretize all partial differentiation terms in the above equation. For example,

$$\left(\frac{\partial\tau_{xx}}{\partial x}\right)_{i,j,k}^{n+1/3} = \frac{\left(\tau_{xx}\right)_{i+1/2,j,k}^{n+1/3} - \left(\tau_{xx}\right)_{i-1/2,j,k}^{n+1/3}}{\left(\Delta x_{i-1} + \Delta x_i\right)/2} \tag{35}$$

where

$$\begin{aligned}\left(\tau_{xx}\right)_{i+1/2,j,k}^{n+1/3} &= \left(\nu + \nu_t\right)\left(\frac{(u_1)_{i+1,j,k}^{n+1/3} - (u_1)_{i,j,k}^{n+1/3}}{\Delta x_i} + \frac{(u_1)_{i+1/2,j,k+1}^{n+1/3} - (u_1)_{i+1/2,j,k-1}^{n+1/3}}{\Delta\sigma_{k-1} + \Delta\sigma_k}\left(\frac{\partial\sigma}{\partial x^*}\right)_{i+1/2,j,k}^{n+1/3}\right)\\ \left(\tau_{xx}\right)_{i-1/2,j,k}^{n+1/3} &= \left(\nu + \nu_t\right)\left(\frac{(u_1)_{i,j,k}^{n+1/3} - (u_1)_{i-1,j,k}^{n+1/3}}{\Delta x_{i-1}} + \frac{(u_1)_{i-1/2,j,k+1}^{n+1/3} - (u_1)_{i-1/2,j,k-1}^{n+1/3}}{\Delta\sigma_{k-1} + \Delta\sigma_k}\left(\frac{\partial\sigma}{\partial x^*}\right)_{i-1/2,j,k}^{n+1/3}\right)\end{aligned} \tag{36}$$

For the pressure propagation step, the projection method [40] is used to calculate the pressure and velocity field,

$$\frac{\left(u_i\right)^{n+1} - \left(u_i\right)^{n+2/3}}{\Delta\tau} = -\left(\frac{1}{\rho}\frac{\partial p}{\partial\xi^k}\frac{\partial\xi^k}{\partial x_i^*}\right)^{n+1} + g_i \tag{37}$$

In detail, Equation (37) can be written as

$$\frac{(u_1)_{i,j,k}^{n+1} - (u_1)_{i,j,k}^{n+2/3}}{\Delta\tau} = -\frac{1}{\rho}\left(\frac{\partial p}{\partial x} + \frac{\partial p}{\partial\sigma}\frac{\partial\sigma}{\partial x^*}\right)_{i,j,k}^{n+1} + g_1 \tag{38}$$

$$\frac{(u_2)_{i,j,k}^{n+1} - (u_2)_{i,j,k}^{n+2/3}}{\Delta\tau} = -\frac{1}{\rho}\left(\frac{\partial p}{\partial y} + \frac{\partial p}{\partial\sigma}\frac{\partial\sigma}{\partial y^*}\right)_{i,j,k}^{n+1} + g_2 \tag{39}$$

$$\frac{(u_3)_{i,j,k}^{n+1} - (u_3)_{i,j,k}^{n+2/3}}{\Delta\tau} = -\frac{1}{\rho}\left(\frac{\partial p}{\partial\sigma}\frac{\partial\sigma}{\partial z^*}\right)_{i,j,k}^{n+1} + g_3 \tag{40}$$

After substituting the aforementioned pressure propagation equation in three directions into the following continuity equation:

$$\frac{\partial(38)}{\partial x} + \frac{\partial(38)}{\partial\sigma}\frac{\partial\sigma}{\partial x^*} + \frac{\partial(39)}{\partial y} + \frac{\partial(39)}{\partial\sigma}\frac{\partial\sigma}{\partial y^*} + \frac{\partial(40)}{\partial\sigma}\frac{\partial\sigma}{\partial z^*} = 0 \tag{41}$$

A modified Poisson equation can be derived [30]. When adopting this method in double-layer σ-coordinate, the Poisson equation has to be changed [35] as follows:

$$\begin{aligned}&\left\{\frac{\partial^2 p}{\partial x^2} + \frac{\partial^2 p}{\partial y^2} + \frac{\partial\sigma}{\partial x^*}\frac{\partial}{\partial\sigma}\left(\frac{\partial\sigma}{\partial x^*}\frac{\partial p}{\partial\sigma}\right) + \frac{\partial\sigma}{\partial y^*}\frac{\partial}{\partial\sigma}\left(\frac{\partial\sigma}{\partial y^*}\frac{\partial p}{\partial\sigma}\right) + \frac{\partial\sigma}{\partial z^*}\frac{\partial}{\partial\sigma}\left(\frac{\partial\sigma}{\partial z^*}\frac{\partial p}{\partial\sigma}\right)\right.\\ &\left. +2\left(\frac{\partial\sigma}{\partial x^*}\frac{\partial^2 p}{\partial x\partial\sigma} + \frac{\partial\sigma}{\partial y^*}\frac{\partial^2 p}{\partial y\partial\sigma}\right) + \left(\frac{\partial^2\sigma}{\partial x^*\partial x} + \frac{\partial^2\sigma}{\partial y^*\partial y}\right)\frac{\partial p}{\partial\sigma}\right\}_{i,j,k}^{n+1}\\ &= \frac{\rho}{\Delta\tau}\left(\frac{\partial u_1}{\partial x} + \frac{\partial u_1}{\partial\sigma}\frac{\partial\sigma}{\partial x^*} + \frac{\partial u_2}{\partial y} + \frac{\partial u_2}{\partial\sigma}\frac{\partial\sigma}{\partial y^*} + \frac{\partial u_3}{\partial\sigma}\frac{\partial\sigma}{\partial z^*}\right)_{i,j,k}^{n+2/3}\end{aligned} \tag{42}$$

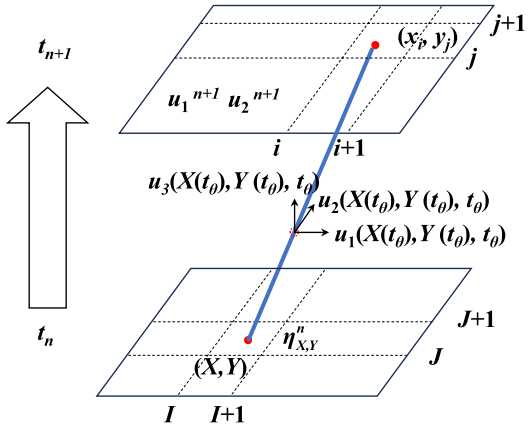

Fig. 2. Sketch of surface tracking method.

The modified Poisson equation is solved by the CGSTAB method [32].

3.2. Surface tracking method

The surface tracking method is presented here, which is different from most other non-hydrostatic models. The kinematic boundary condition of the moving surface, as defined in Equation (20), is an advection equation. It can be solved by the characteristics method, specifically the Lagrangian–Eulerian method. Fig. 2 illustrates that the original position of particles (X, Y) at nth time step can be determined by tracking the Lagrangian movement of particles at point (x_i, y_j) at the $(n+1)$th time step using Lagrangian displacement equations:

$$x_i - X = \int_{t_n}^{t_{n+1}} u_1(X(t), Y(t), t)\, dt = u_1\left(X(t_\theta), Y(t_\theta), t_\theta\right) \Delta t \tag{43}$$

$$y_j - Y = \int_{t_n}^{t_{n+1}} u_2(X(t), Y(t), t)\, dt = u_2\left(X(t_\theta), Y(t_\theta), t_\theta\right) \Delta t \tag{44}$$

where $\Delta t = t_{n+1} - t_n$ is the time step and $t_\theta = t_n + \theta \Delta t$ is an intermediate point between t_{n+1} and t_n, θ ranges from 0 to 1 and is set as 0.5 in the simulation.

Equation (43) and Equation (44) can be further expanded using Taylor series expansion at point (x_i, y_j) as

$$x_i - X = u_1\left(X(t_\theta), Y(t_\theta), t_\theta\right) \Delta t = \left\{ {u_1}_{i,j}^{n+1} - \theta \left(\frac{\partial u_1}{\partial x}\right)_{i,j}^{n+1} (x_i - X) - \theta \left(\frac{\partial u_1}{\partial y}\right)_{i,j}^{n+1} (y_j - Y) - \theta \left(\frac{\partial u_1}{\partial t}\right)_{i,j}^{n+1} \Delta t \right\} \Delta t \tag{45}$$

$$y_j - Y = u_2\left(X(t_\theta), Y(t_\theta), t_\theta\right) \Delta t = \left\{ {u_2}_{i,j}^{n+1} - \theta \left(\frac{\partial u_2}{\partial x}\right)_{i,j}^{n+1} (x_i - X) - \theta \left(\frac{\partial u_2}{\partial y}\right)_{i,j}^{n+1} (y_j - Y) - \theta \left(\frac{\partial u_2}{\partial t}\right)_{i,j}^{n+1} \Delta t \right\} \Delta t \tag{46}$$

Upon applying the central difference scheme to the spatial differential terms and the forward difference scheme to the temporal differential terms, the variables (X, Y) can be easily obtained by solving Equation (45) and Equation (46). Assuming the particle is located within the element (I, J) at time t_n. The original surface elevation $\eta^n_{X,Y}$ can be estimated using either linear or higher-order interpolation based on the grid node values within the element (I, J). Subsequently, employing the Lagrange displacement equation once more, the surface elevation at the subsequent time step t_{n+1} can be updated using the following formula:

$$\eta_{i,j}^{n+1} = \eta^n_{X,Y} + \left\{ {u_3}_{i,j}^{n+1} - \theta \left(\frac{\partial u_3}{\partial x}\right)_{i,j}^{n+1} (x_i - X) - \theta \left(\frac{\partial u_3}{\partial y}\right)_{i,j}^{n+1} (y_j - Y) - \theta \left(\frac{\partial u_3}{\partial t}\right)_{i,j}^{n+1} \Delta t \right\} \Delta t \tag{47}$$

3.3. Stability criteria

Since explicit schemes are used to discretize the advection and diffusion terms in the momentum equations, the maximum time step must be limited to ensure the stability of the numerical schemes [30]. As for the advection process, the time step is limited by the Courant-Friedrichs-Lewy (CFL) condition as follows:

$$\Delta t \le \gamma \cdot max\left(\frac{{\Delta x_i}^*}{(u_i)_{max}}\right) \tag{48}$$

where $i = 1, 2, 3$ and $(u_i)_{max}$ is the maximum particle velocity in the horizontal, transverse, or vertical direction, respectively. The theoretical value of γ is 1.0, but it is set below 0.2 to ensure accuracy and stability within the computational domain in the model.

Another stability constraint goes to the diffusion process. According to the stability analysis, the following conditions must be satisfied:

$$\Delta t \leq \chi \cdot \frac{(\Delta x_i^*)^2}{\nu} \tag{49}$$

where χ is set as 0.2. While in most of the cases we studied, the maximum allowable time step is restricted by Equation (48).

4. Results and discussion

In this section, the capabilities of the double-layer σ model are evaluated using seven test cases and compared with a single-layer σ model. These test cases encompass solitary and regular wave propagation without and with structures and the horizontal jet in stagnant and wave environments. All simulations were carried out on a desktop computer with an AMD Ryzen(TM) 9 7900X CPU and 32GB internal memory. The base frequency of this CPU is 4.7 GHz.

4.1. Wave mechanics

4.1.1. Solitary waves

The propagation of a solitary wave in a constant water depth is a classic test, which is often used as a preliminary assessment before exploring wave or wave-structure interactions. In this study, the computational area is 100 m in length and 1 m in depth. In the double-layer σ model, the depth in the bottom layer is set as $h_1 = 0.1$ m, while the upper layer depth is $h_2 = 0.9$ m. The amplitude of the solitary wave H is set to 0.1 m. The time history of free surface displacement and velocities are specified at inflow boundary as [50,51]:

$$\eta(t) = H\,\mathrm{sech}^2(\theta) \tag{50}$$

$$\frac{u_1(z,t)}{\sqrt{gh}} = \frac{\eta(t)}{h} - \frac{\eta^2(t)}{4h^2} - \frac{1}{2}\left(\frac{H}{h}\right)^2\left(1 - \frac{3}{2}\frac{z^2}{h^2}\right)\left(-2\,\mathrm{sech}^2(\theta) + 3\,\mathrm{sech}^4(\theta)\right) \tag{51}$$

$$\frac{u_3(z,t)}{\sqrt{gh}} = -\frac{z}{h}\frac{2H}{\Delta}\left[1 - \frac{\eta(t)}{2h} + \frac{H}{h}\left(1 - \frac{z^2}{2h^2}\right)\left(1 - 3\,\mathrm{sech}^2(\theta)\right)\right]\tanh(\theta)\cdot\mathrm{sech}^2(\theta) \tag{52}$$

where $\theta = \frac{(x_s - Ct)}{\Delta}$; x_s represents the initial position of the solitary wave and is defined as $x_s = \frac{4h}{\sqrt{\frac{H}{h}}}$; wave celerity C is set to $\sqrt{gh\left(1 + \frac{H}{h}\right)}$ and $\Delta = h\sqrt{\frac{4h}{3H}}$.

As the propagation of a solitary wave in a flume has an analytical solution, we conducted tests based on this scenario to verify the convergence order of our model. The normalized L_1 error E_{L_1}, L_2 error E_{L_2}, and maximum error E_{L_∞} were used in this test. These errors are calculated as follows:

$$E_{L_1} = \frac{\sum\left|\eta_{numerical} - \eta_{analytical}\right|}{n} \tag{53}$$

$$E_{L_2} = \sqrt{\frac{\sum(\eta_{numerical} - \eta_{analytical})^2}{n}} \tag{54}$$

$$E_{L_\infty} = max\left|\eta_{numerical} - \eta_{analytical}\right| \tag{55}$$

First, the domain is discretized using a base grid with uniform sizes $\Delta x = 0.1$ m and $\Delta z = 0.01$ m. The turbulence model is switched off, and the time step is set to a very small value (i.e., 0.000125 s) to verify the spatial order of the model. Six different sets of grids are used, each with a uniform grid size in the vertical direction ($\Delta z = 0.01$ m) and varying horizontal grid sizes Δx (as shown in Table 1). The L_1 error (E_{L_1}), L_2 error (E_{L_2}), and maximum error (E_{L_∞}) are also calculated. The results in Fig. 3 indicate that the convergence order in the horizontal direction is first order. For the vertical direction, the water depth is discretized into 5, 10, 20, 30, 40, 50, and 100 grids (as shown in Table 2). The errors decrease when discretized by 5 or 10 grids but tend to stabilize after 20 grids, indicating that fewer grids are needed when using σ transformation in the vertical direction. Additional simulations with a finer horizontal grid (smaller Δx) have confirmed that the error reduction is primarily influenced by the vertical discretization, as further refinement in the horizontal direction do not result in notable improvements (Fig. 3).

Furthermore, a temporal convergence study was conducted using six different time steps Δt with a uniform grid size of $\Delta x = 0.1$ m and $\Delta z = 0.01$ m. The results are shown in Fig. 4 and Table 3. The temporal convergence order is close to the first order, which is consistent with the scheme used for the time integration. Finally, a uniform grid size of $\Delta x = 0.1$ m and $\Delta z = 0.01$ m with $\Delta t = 1.25 \times 10^{-4}$ s were selected for the simulation in this case.

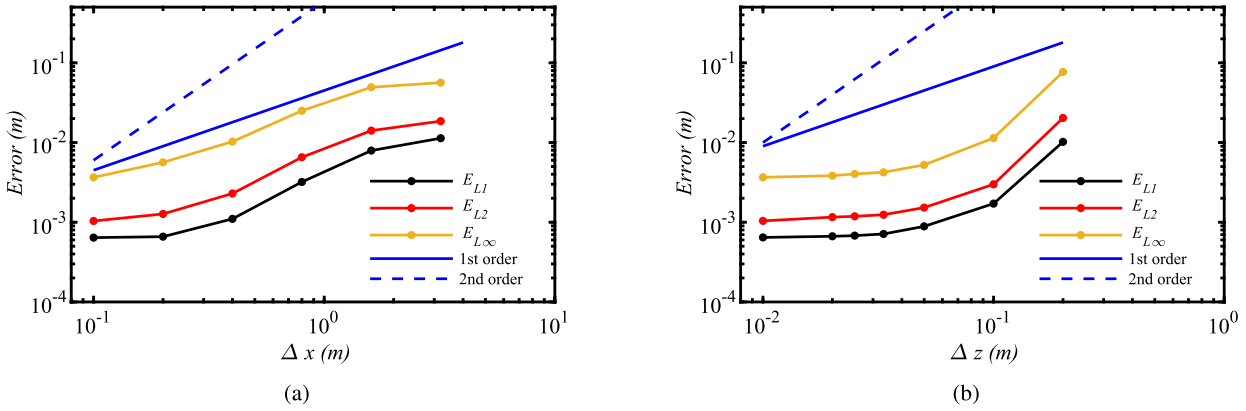

Fig. 3. Spatial convergence study of the solitary wave along the whole flume at $t = 20$ s: (a) horizontal direction; (b) vertical direction.

Table 1
Spatially convergence test in the horizontal direction.

Δx (m)	E_{L_1} (m)	E_{L_2} (m)	E_{L_∞} (m)
3.2	1.13×10^{-2}(-)	1.86×10^{-2}(-)	5.64×10^{-2}(-)
1.6	7.93×10^{-3}(0.52)	1.41×10^{-2}(0.39)	4.94×10^{-2}(0.19)
0.8	3.20×10^{-3}(1.31)	6.54×10^{-3}(1.11)	2.51×10^{-2}(0.98)
0.4	1.10×10^{-3}(1.54)	2.29×10^{-3}(1.51)	1.03×10^{-2}(1.28)
0.2	6.59×10^{-4}(0.74)	1.27×10^{-3}(0.85)	5.64×10^{-3}(0.87)
0.1	6.45×10^{-4}(0.04)	1.04×10^{-3}(0.29)	3.66×10^{-3}(0.62)

Table 2
Spatially convergence test in the vertical direction.

Δz (m)	E_{L_1} (m)	E_{L_2} (m)	E_{L_∞} (m)
0.2	1.02×10^{-2}(-)	2.03×10^{-2}(-)	7.69×10^{-2}(-)
0.1	1.68×10^{-3}(2.57)	2.99×10^{-3}(2.76)	1.14×10^{-2}(2.76)
0.05	8.87×10^{-4}(0.95)	1.53×10^{-3}(0.97)	5.24×10^{-3}(1.12)
0.033	7.13×10^{-4}(0.54)	1.24×10^{-3}(0.51)	4.23×10^{-3}(0.53)
0.025	6.79×10^{-4}(0.17)	1.19×10^{-3}(0.16)	4.04×10^{-3}(0.16)
0.02	6.67×10^{-4}(0.08)	1.16×10^{-3}(0.10)	3.84×10^{-3}(0.22)
0.01	6.45×10^{-4}(0.05)	1.04×10^{-3}(0.15)	3.66×10^{-3}(0.07)

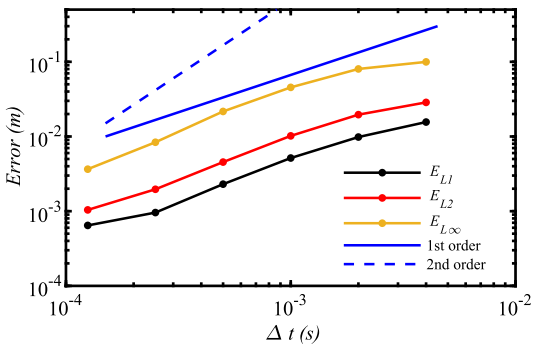

Fig. 4. Temporal convergence study of the solitary wave propagation.

Fig. 5 shows a comparison of the numerical simulations against analytical results. Sub-figures 5(a), (b), (c) display the comparison of free-surface elevation, middle-depth horizontal velocity, and vertical velocity at $t = 10$, 20 and 30 s, respectively. The outcomes demonstrate a good agreement between the numerical results and analytical solutions.

Table 3
Temporal convergence test.

Δt (s)	E_{L_1} (m)	E_{L_2} (m)	E_{L_∞} (m)
4×10^{-3}	1.56×10^{-2}(-)	2.86×10^{-2}(-)	9.97×10^{-2}(-)
2×10^{-3}	9.83×10^{-3}(0.67)	1.96×10^{-2}(0.55)	8.02×10^{-2}(0.32)
1×10^{-3}	5.15×10^{-3}(0.93)	1.02×10^{-2}(0.94)	4.55×10^{-2}(0.82)
5×10^{-4}	2.30×10^{-3}(1.16)	4.54×10^{-3}(1.17)	2.16×10^{-2}(1.07)
2.5×10^{-4}	9.58×10^{-4}(1.26)	1.96×10^{-3}(1.21)	8.37×10^{-3}(1.00)
1.25×10^{-4}	6.45×10^{-4}(0.57)	1.04×10^{-3}(0.61)	3.66×10^{-3}(0.74)

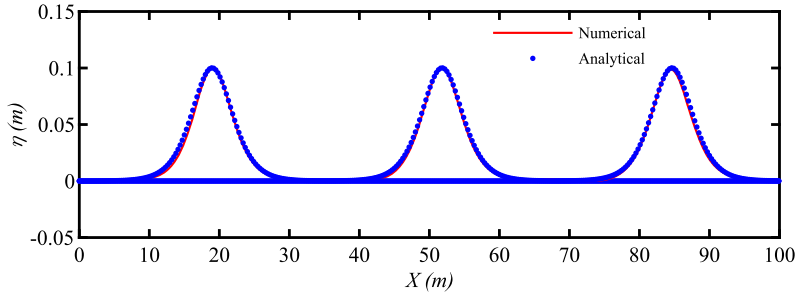

(a) Free-surface elevation

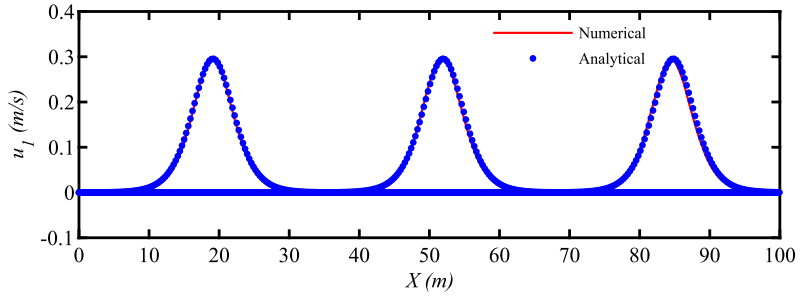

(b) Horizontal velocity at middle depth

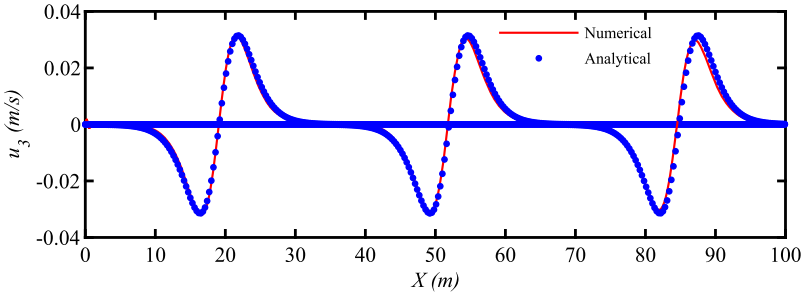

(c) Vertical velocity at middle depth

Fig. 5. Validation of the calculated and analytical (a) free-surface elevation, (b) horizontal velocity at middle depth and (c) vertical velocity at middle depth using the double-layer model at $t = 10$, 20 and 30 s (from left to right).

4.1.2. Regular waves

A test on the regular wave is then conducted in the numerical wave flume. For this simulation, the flume has a length of 15 m, a width of 0.5 m, and a depth of 0.5 m. The damping zone is set as 5 m in length. The amplitude of the wave is 0.004 m, and the wave period is 1 s, which corresponds to Airy's wave theory. The computational domain is discretized by a $301\times11\times100$ mesh. The grid size is uniform with $\Delta x = 0.05$ m in the x direction, $\Delta y = 0.05$ m in the y direction. While in the σ direction, a non-uniform grid is adopted with minimum value $\Delta\sigma = 0.0015$ near the surface.

To examine the effect of bottom layer thickness on the simulation cases, eleven different bottom layer water depths (corresponding to σ values ranging from 0 to 0.96) are selected and the results are compared with analytical results from Airy's wave theory [52],

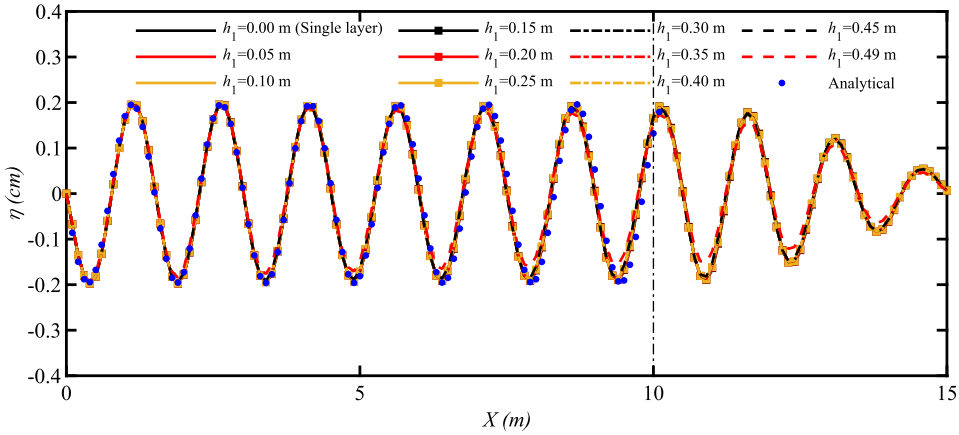

Fig. 6. The effect of different bottom and top layer thickness for regular waves in the numerical wave tank.

Table 4
The error table on the effect of different bottom and top layer thickness for regular waves in the numerical wave tank.

h_1 (m)	E_{L_1} (cm)	E_{L_2} (cm)	E_{L_∞} (cm)	H (cm) (ε_H)
0.00 ($\alpha = 0.0$)	0.0141	0.0187	0.048	0.3918 (2.04%)
0.05 ($\alpha = 0.1$)	0.0144	0.0192	0.049	0.3917 (2.07%)
0.10 ($\alpha = 0.2$)	0.0146	0.0194	0.050	0.3902 (2.46%)
0.15 ($\alpha = 0.3$)	0.0151	0.0201	0.052	0.3900 (2.50%)
0.20 ($\alpha = 0.4$)	0.0155	0.0206	0.053	0.3895 (2.63%)
0.25 ($\alpha = 0.5$)	0.0158	0.0211	0.054	0.3891 (2.71%)
0.30 ($\alpha = 0.6$)	0.0159	0.0212	0.054	0.3883 (2.93%)
0.35 ($\alpha = 0.7$)	0.0160	0.0214	0.054	0.3880 (3.00%)
0.40 ($\alpha = 0.8$)	0.0164	0.0220	0.056	0.3871 (3.23%)
0.45 ($\alpha = 0.9$)	0.0180	0.0242	0.062	0.3855 (3.62%)
0.49 ($\alpha = 0.98$)	0.0205	0.0265	0.070	0.3615 (9.63%)

as shown in Fig. 6. The error table is presented in Table 4. In this case, the relative error in wave height (ε_H) is calculated as follows:

$$\varepsilon_H = \frac{\left| H_{numerical} - H_{analytical} \right|}{H_{analytical}} \times 100\% \tag{56}$$

It is found that when σ changes from 0 to 0.9, no significant differences are observed in several cases. However, when the thickness of the bottom layer approaches the total water depth (i.e., the upper layer water depth approaches the wave height), a distinct decrease in wave height can be observed, and the relative error compared to the analytical results increases significantly. Fig. 7 shows the relative volume of water over time in the numerical wave tank. The volume of water in the flume is well-preserved and stabilizes after 30 seconds, and no significant decrease in relative water volume is observed. Additionally, it can be concluded that as the water depth in the bottom layer increases, the time history of the relative volume of water is very similar, which is consistent with the aforementioned pattern.

4.2. Wave-structure interaction

4.2.1. Solitary waves pass a submerged obstacle

When a solitary wave interacts with a submerged rectangular obstacle, vortices emerge on both the windward and leeward sides of the obstacle, persisting for an extended period. This phenomenon is especially relevant for evaluating the accuracy of Navier-Stokes Equation (NSE) models in capturing flow patterns associated with vortices around structures, and it has been thoroughly investigated through numerical studies.

The sketch of this problem is shown in Fig. 8. The water depth is 0.228 m and the wave height is 0.069 m. The obstacle, which is 0.114 m in height and 0.381 m in length, is placed 2.619 m downward of the inflow boundary. Two gauging points are placed behind the obstacle: Point 1 is located 0.04 m above the bottom and 0.034 m downstream from the obstacle, while Point 2 is 0.017 m above Point 1 [53]. The computational domain is discretized by a $2881 \times 3 \times 101$ uniform grid with $\Delta x = 0.0025$ m, $\Delta y = 0.0025$ m and $\Delta\sigma = 0.01$. In the double-layer σ model, the depth in the bottom layer is set as $h_1 = 0.114$ m, and the depth in the upper layer is set as $h_2 = 0.114$ m. The simulation uses a time step of 0.002 s and the total CPU time per time step required for the present model was about 1.48 s.

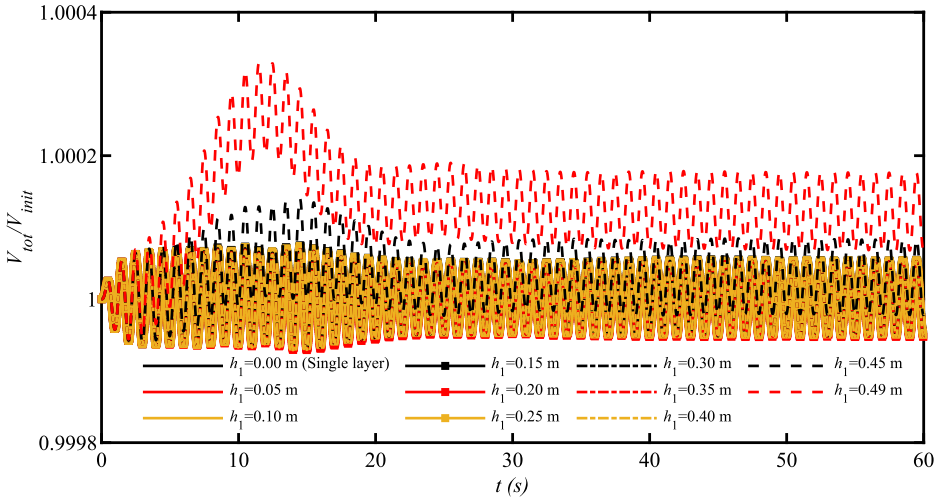

Fig. 7. Relative volume of water over time for regular waves in the numerical wave tank.

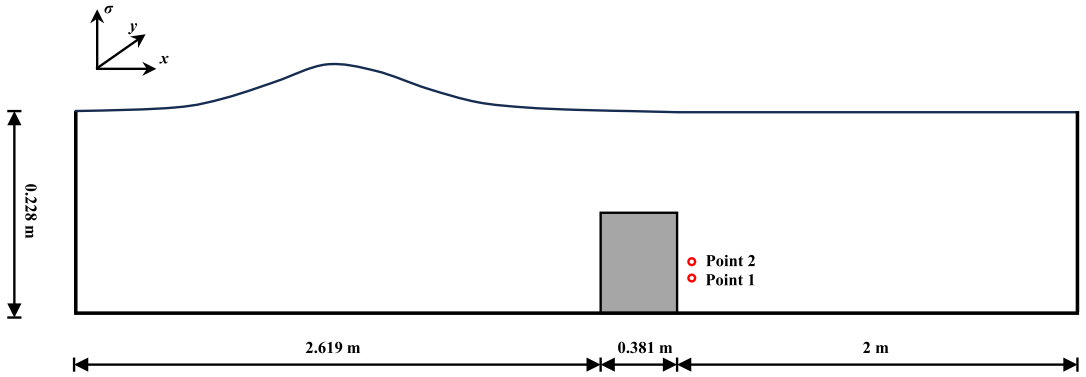

Fig. 8. Sketch of solitary wave propagation over a submerged rectangular obstacle.

Fig. 9 compares the time histories of horizontal and vertical velocities at two gauging points among the single-layer model, the present double-layer model, and the experimental data by Zhuang and Lee [53]. The water depth in the bottom layer (h_1) varies from 0.114 m (i.e., $\alpha = 0.5$ and equal to the obstacle upper surface) to 0.2052 m (i.e., $\alpha = 0.9$). It is found that both the single-layer and double-layer models can capture the velocity trend at the gauging points. Notably, the double-layer model aligns more closely with the experimental results than the single-layer model. Additionally, it is observed that the horizontal and vertical velocities at the two gauging points do not change significantly with different bottom layer water depths.

Fig. 10 shows the flow fields and free surface profiles around the obstacle at several representative times using both the single-layer model and the double-layer model. It can be seen from these figures that when using the single-layer model, the upper surface shape of the obstacle varies with changes in water surface elevation, resulting in continuous changes in the location and size of the vortices. This variation is likely to account for the observed differences in the time histories of horizontal and vertical velocities between these two models shown in Fig. 9. In contrast, the upper surface shape of the obstacle would not change in the double-layer model, and the position of the vortex formed near the obstacle corresponds well with previous research [22,35].

4.2.2. Regular wave pass a submerged plate

In coastal and ocean engineering, a common simplification is to represent various structures as fully submerged horizontal plates. These structures often include plate-type breakwaters, semi-submersible very large floating structures (VLFS), and plate-type wave energy converters (WECs). Submerged plates offer a cost-effective solution for coastal regions, minimally impacting the dynamics of nearshore currents and sediment transportation, among other environmental factors. In this case, the developed model is used to reproduce the experiment by Dong et al. [54].

A schematic view of the numerical setup is shown in Fig. 11. The wave flume has a length of 60 m, a width of 0.8 m, and a depth of 0.5 m. The submerged plate is 2 m in length, 0.78 m in width, and 0.1 m in thickness. Four gauging points are placed in the flume, two in front of the plates and two behind the plates. The wave height is 0.05 m and the wave period is 1.4 s. However, we find the

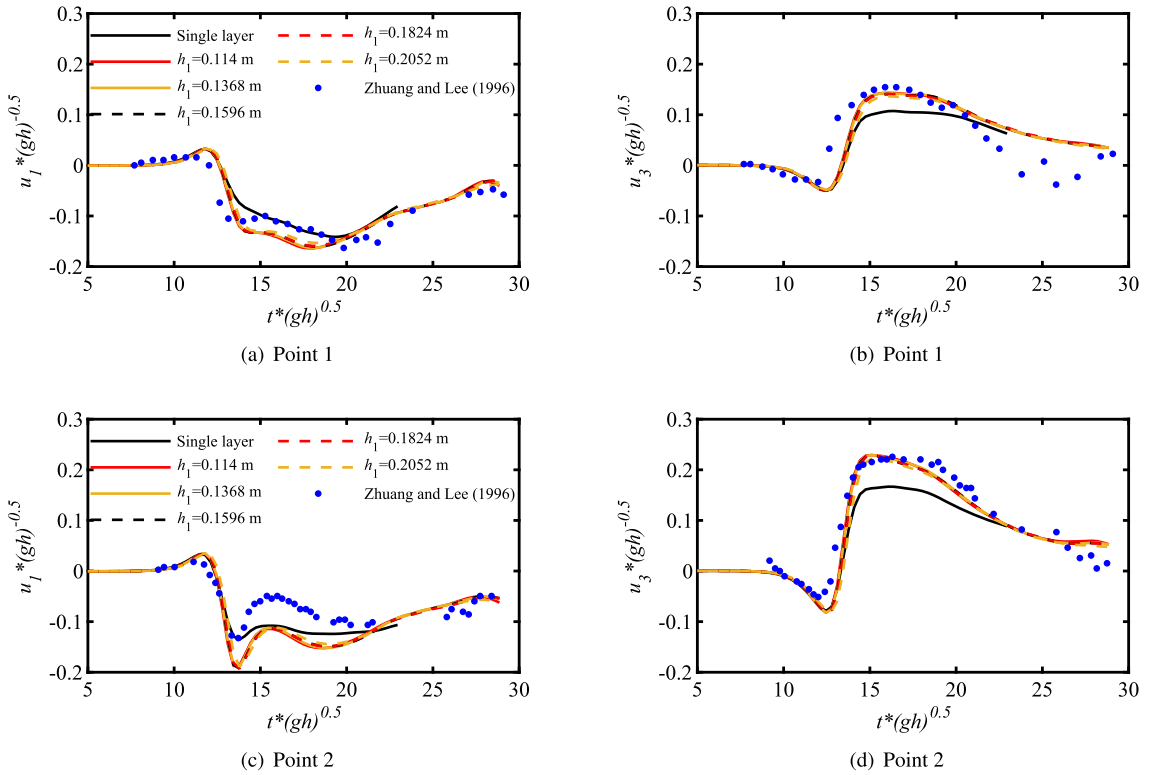

Fig. 9. Comparisons of time histories of horizontal and vertical velocities at two points among single-layer model, present double-layer model and experimental data.

elevation changes in the data shown in Dong et al. [54] are larger than 5 cm. It is also mentioned in the article that the input wave height for the wavemaker signal is a bit larger than the expected wave height because of the viscosity and friction against the sidewall and bottom. Consequently, in our simulation, we choose to set the wave height to 7 cm at the inflow boundary. The computational domain has the same size as the experiments and is discretized into a $1201 \times 17 \times 101$ uniform grid with $\Delta x = 0.05$ m, $\Delta y = 0.05$ m and $\Delta\sigma = 0.01$. The depth in the bottom layer is set as $h_1 = 0.4$ m, and the depth in the upper layer is set as $h_2 = 0.1$ m in order to keep the shape of the structure fixed, as shown in the previous case. The time step is set to 0.002 s and the total CPU time per time step required for the present model is about 2.6 s.

Fig. 12 shows the time history of free-surface elevation at four gauging points between numerical results and experimental data. The numerical results closely align with the experimental data, though a minor phase difference is observed. These phase differences can be partly attributed to the grid solution, as highlighted in Chen et al. [55], which suggests that the grid size at the surface should be sufficiently small to avoid introducing phase difference in the simulation when using this Lagrangian-Eulerian method. Overall, the developed double-layer σ-coordinate model effectively simulates regular wave-structure interactions and nonlinear effects.

Fig. 13 presents some snapshots of top views for 3D free surface elevation, illustrating the propagation process of regular waves over a submerged plate, which is delineated by a red rectangle. At time 44.5 s, the wave peak is approaching the front part of the plate, where noticeable wave deformation occurs. Thereafter, at time 44.9 s, as the wave traverses the plate, two prominent high points, resulting from wave deformation are observed in the elevation data. By 45.4 seconds, the wave has completely passed the plate, leaving a single prominent high point visible in the elevation.

4.2.3. Regular wave passes a submerged bar

We have conducted numerous numerical simulations to evaluate the performance of the double-layer model under wave conditions. While in the initial cases, the water depth in both layers was kept constant along the horizontal direction. To assess the model's capability in simulating scenarios with varying water depths along the flume, we simulated a case where a wave passes over a submerged bar, based on experiments conducted by Beji and Battjes [56].

The experimental setup is illustrated in Fig. 14. The flume is 30 m long, 0.5 m wide, and has a water depth of 0.4 m. The regular wave has a height of 0.02 m and a period of 1 s. The computational domain is discretized using a non-uniform mesh with 2637 grids in the x-direction, 11 grids in the y-direction, and 47 grids in the σ-direction. The smallest grid size near the surface is less than 0.006 m, and a time step of $\Delta t = 0.002$ s is chosen and the total CPU time per time step required for the present model was about 1.8 s. Similar to the previous cases, we varied the separation position of the two layers. The separation position ranged from $\alpha = 0.2$ to $\alpha = 0.8$ in intervals of $\Delta\alpha = 0.2$. For comparison, a single-layer model was also used.

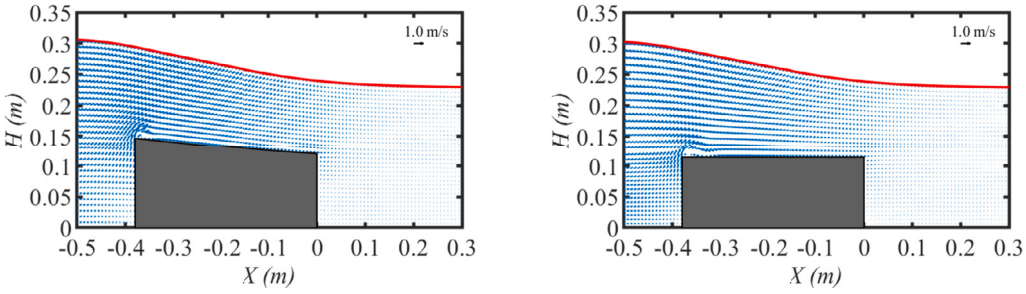

(a) $t\sqrt{g/h}$ = 10.49 (Single layer)

(b) $t\sqrt{g/h}$ = 10.49 (Double layer)

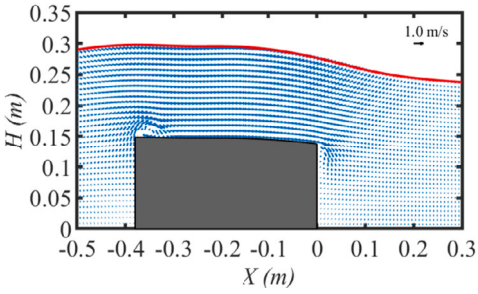

(c) $t\sqrt{g/h}$ = 11.80 (Single layer)

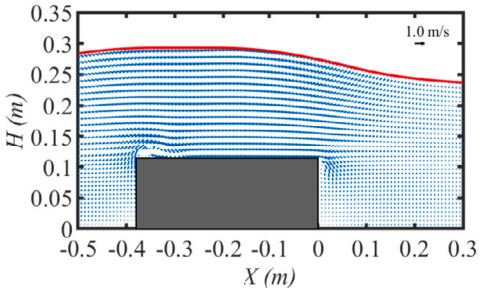

(d) $t\sqrt{g/h}$ = 11.80 (Double layer)

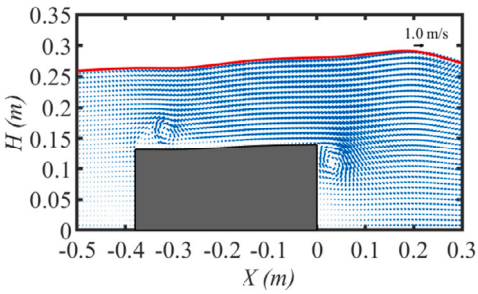

(e) $t\sqrt{g/h}$ = 13.11 (Single layer)

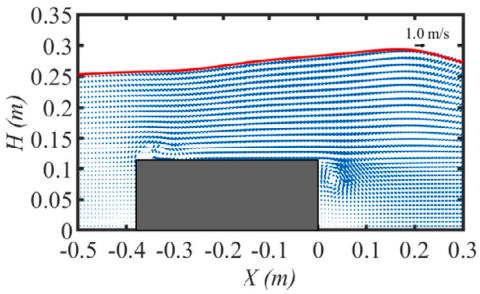

(f) $t\sqrt{g/h}$ = 13.11 (Double layer)

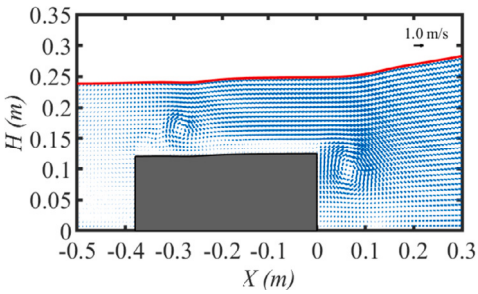

(g) $t\sqrt{g/h}$ = 14.43 (Single layer)

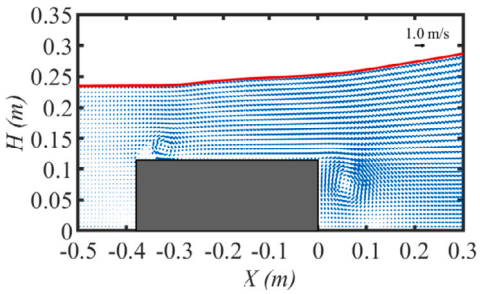

(h) $t\sqrt{g/h}$ = 14.43 (Double layer)

Fig. 10. Velocity fields and free surface profiles around the obstacle at several representative times using single layer and double layer σ model (Left column: Single layer; Right column: Double layer).

To facilitate a comparison, we acquired experimental data by digitizing the diagrams presented by Yuan and Wu [57]. Fig. 15 compares our numerical results with the experimental data for free surface elevation at four gauging points. At wave gauge 1 (x = 5.7 m), the wave retains its sinusoidal shape. As the wave propagates from x = 6.0 m to x = 12.0 m, deformation occurs at Gauge 2 (x = 10.5 m) as it climbs the slope. At wave gauges 3 (x = 12.5 m) and 5 (x = 14.5 m), where the wave surmounts the breakwater, secondary wave growth becomes evident. Additionally, as the depth in the bottom layer increases, the numerical results remain consistent, further confirming the model's stability.

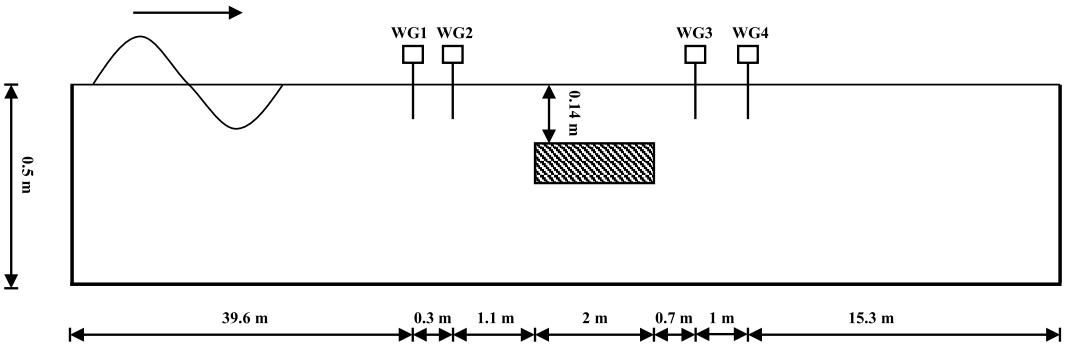

Fig. 11. Sketch of regular wave propagation over a submerged rectangular plate.

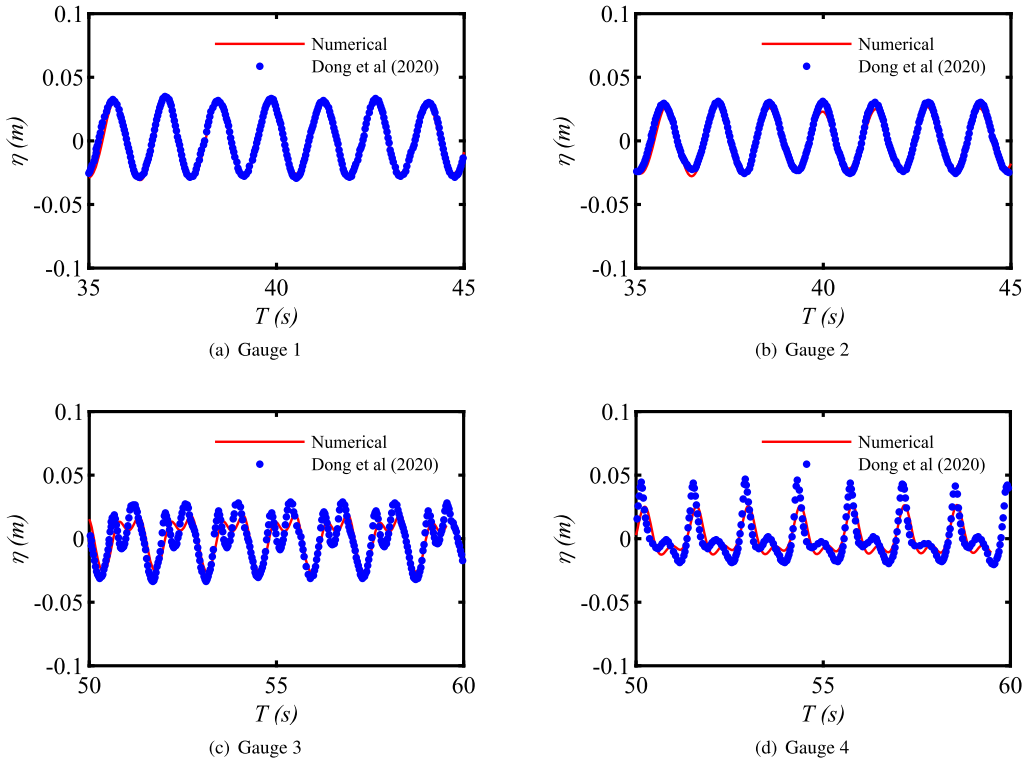

Fig. 12. Time history of wave passing a submerged plate at four gauging points.

4.3. Wave-jet interaction

4.3.1. Horizontal jet in stagnant environment

To simulate the flow pattern of a horizontal jet under wave conditions, it is essential to first examine the jet's behavior in stagnant conditions. Additionally, as previously mentioned, the Synthetic-Eddy-Method (SEM) is also employed, so the validation of the selected parameters used in the jet's outflow boundary condition is very important.

The setup of this case is the same as the experiments performed by Chen et al. [58]. The hydrostatic water depth is 0.6 m. The horizontal jet is set at the middle water depth. The computational domain is discretized into a $131 \times 41 \times 139$ grid. The non-uniform grid is used with minimum $\Delta x = 0.0886$ m, minimum $\Delta y = 0.0886$ m and $\Delta \sigma = 0.002$. As the water depth is kept constant in the flume, the depth in the bottom layer is set as $h_1 = 0.02$ m, and the depth in the upper layer is set as $h_2 = 0.58$ m for simplicity. The jet orifice is divided by a 11×11 grid system. The outflow velocity is 0.88 m/s, the time step is also taken as 0.002 s, and the total CPU time per time step required for the present model was about 5.8 s.

Fig. 16 shows the centerline velocity decay and the axial velocity distribution of jet in stagnant and its comparison with both commonly acknowledged empirical solution and experiment data performed by other researchers [59]. The figure indicates that the

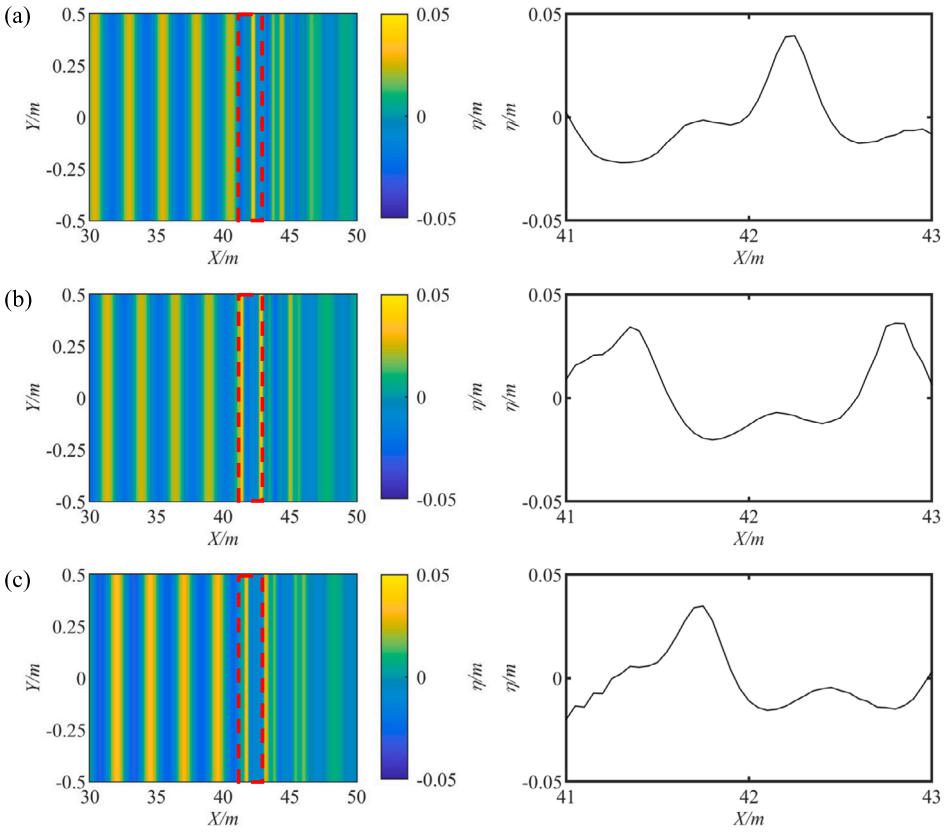

Fig. 13. 3D top (left panels) and side (right panels) view plots of free surface elevation at several representative times: (a) $T = 44.5$ s, (b) $T = 44.9$ s, (c) $T = 45.3$ s. (For interpretation of the colors in the figure(s), the reader is referred to the web version of this article.)

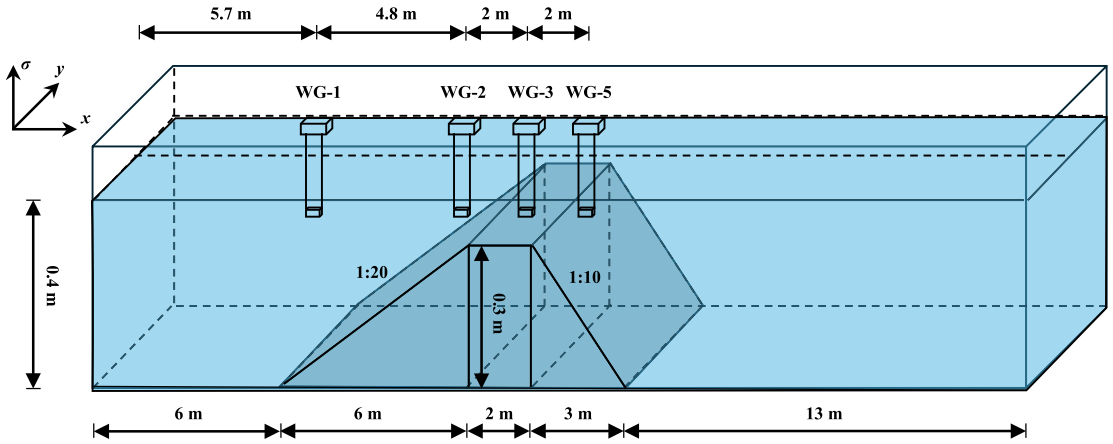

Fig. 14. Sketch of periodic regular wave propagation over a submerged bar with varying water depth.

simulated results correspond closely with the experimental results, and the velocity distribution at various cross-sections follows the Gaussian distribution.

The distribution of axial turbulence intensities and Reynolds stress normalized by the square of the axial centerline velocity at x/d =20 is shown in Fig. 17. These distributions are also compared with experiments conducted by Hussein et al. [60] and numerical simulation by Bogey and Bailly [61]. The results from the SEM method show substantial agreement with both the experimental and numerical data. It is worth noting that the statistically turbulent quantities depicted in the figure are in the far field of the jet, where the jet enters its turbulent self-similar zone. Consequently, the simulated turbulence properties exhibit less congruence in the near field of the jet.

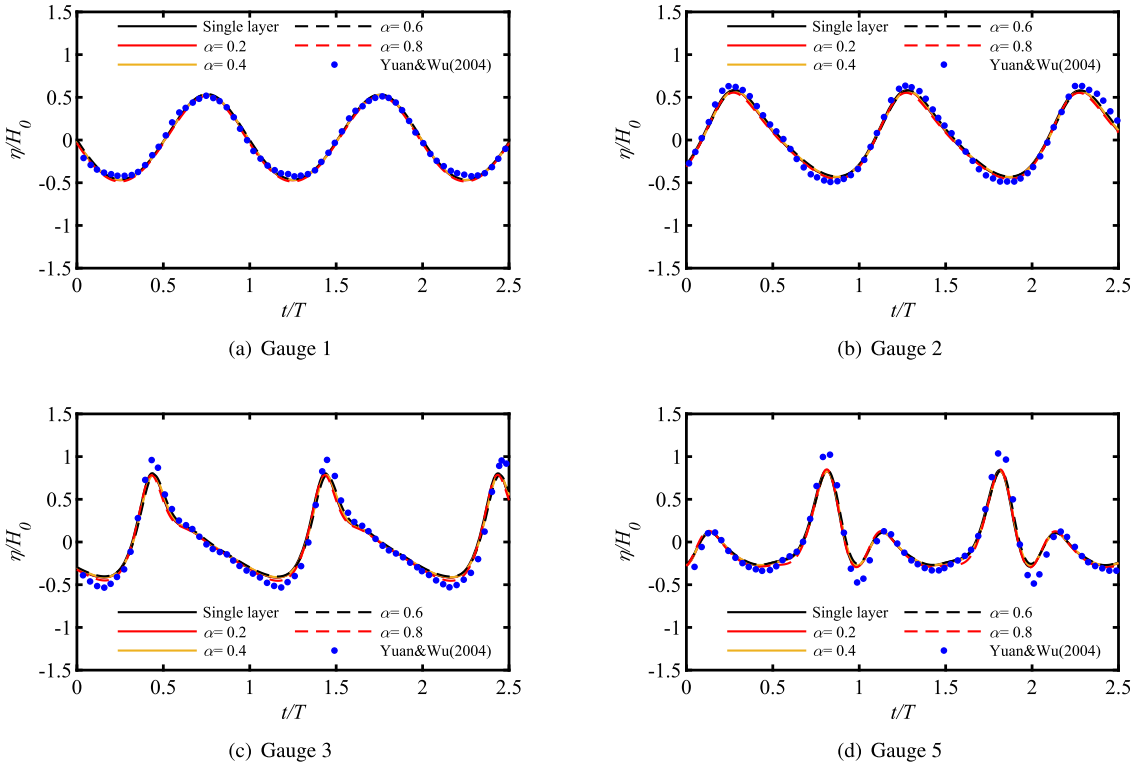

Fig. 15. Time history of the wave passing a submerged bar at four gauging points.

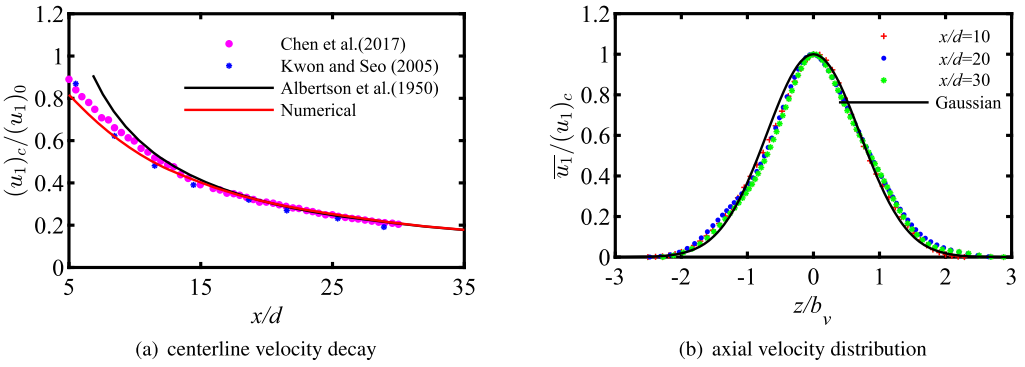

Fig. 16. Comparison of (a) centerline velocity decay; (b) axial velocity distribution (b_v means jet Gaussian half-width) between experiments and numerical simulations.

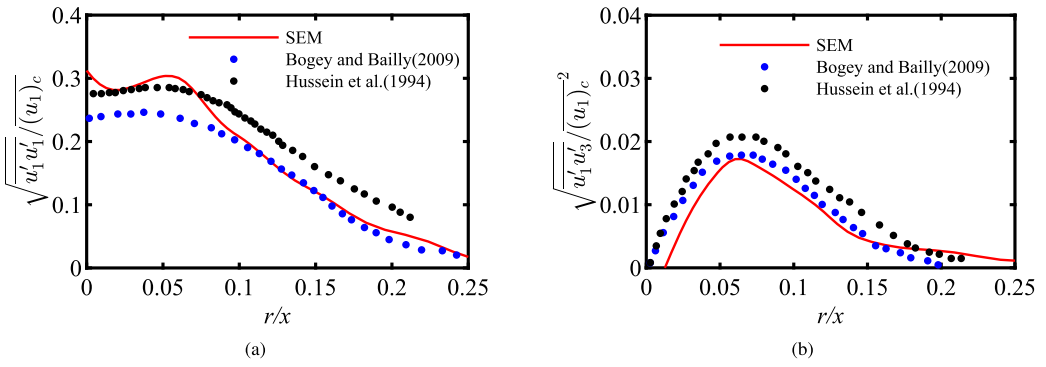

Fig. 17. Comparison of the distribution of (a) axial turbulence intensity; (b) normalized Reynolds stress between experiments and numerical simulation at $x/d = 20$.

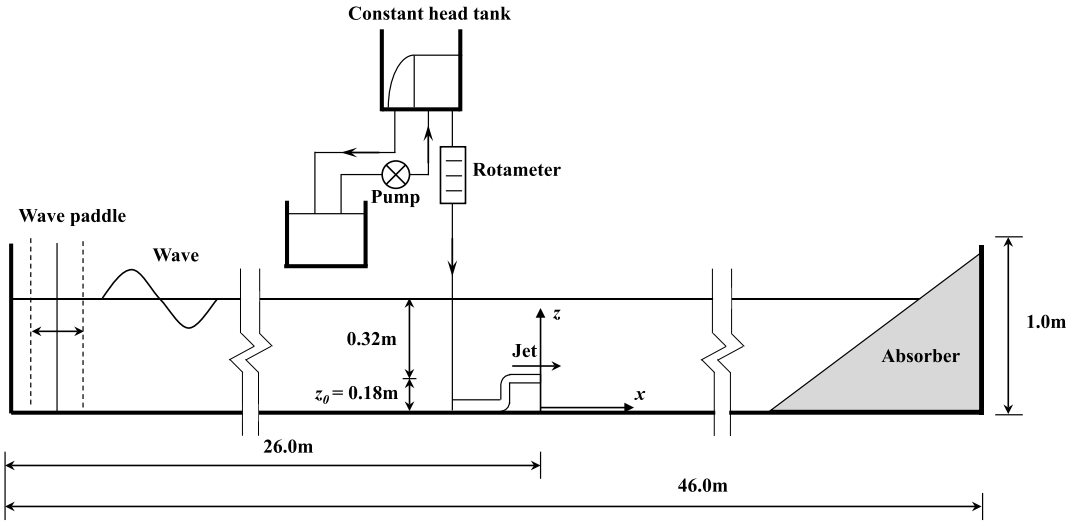

Fig. 18. Sketch of jet in waves.

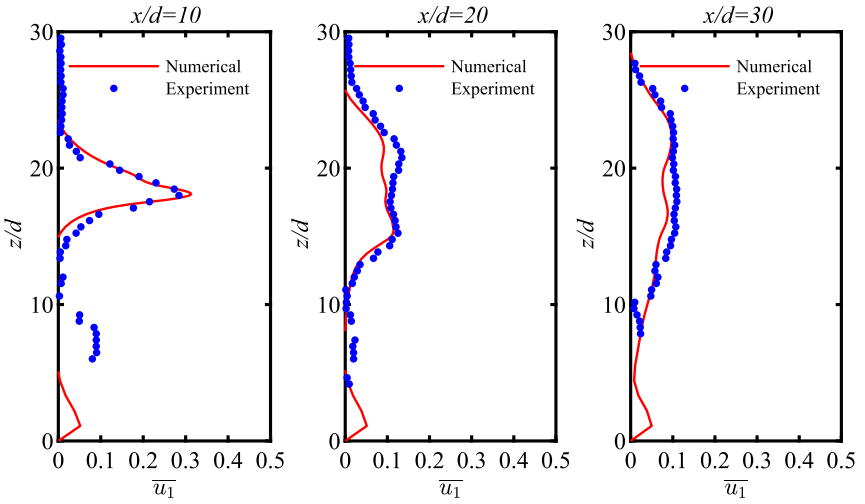

Fig. 19. Comparison of axial velocity between numerical simulation results and experiment results at three different cross-sections.

4.3.2. Horizontal jet in wave environment

In this study, we conducted simulations to analyze the flow patterns of a horizontal jet in wave conditions. The sketch of the experiment is shown in Fig. 18. The flume dimensions are 46 m in length, 0.5 m in width, and 1.0 m in depth. A piston-type wave generator is installed at one end of the flume, and an absorber, which is used to dissipate wave energy and minimize reflections, is installed at another end. The still water depth is maintained at 0.5 m in the experiments. A horizontal jet is introduced via a 0.01 m diameter acrylic nozzle and is 0.18 m above the flume bottom. In terms of simulation parameters, the computational domain has a length of 15 m, a width of 0.5 m, and a depth of 0.5 m and is discretized into a grid system of $368 \times 41 \times 139$. The bottom layer depth is set at $h_1 = 0.3$ m, and the upper layer at $h_2 = 0.2$ m. The damping zone is set as 5 m in length. The chosen wave period and height are 1.5 s and 0.06 m, respectively. A time step of 0.002 s is used in the simulation and the total CPU time per time step required for the present model was about 9.6 s. The outflow velocity of the horizontal jet is set as 0.85 m/s.

Fig. 19 shows the comparison of the time-averaged axial velocity between numerical simulations and experimental results at three different cross-sections. The numerical results show a good agreement with the experiments, and both the 'single-peaked' pattern and the 'twin-peaked' pattern can be clearly observed in the figures. In the near-field region, the jet's behavior is primarily influenced by its initial momentum, resulting in a 'single-peaked' velocity distribution. Conversely, as the jet progresses downstream, its momentum diminishes, and wave effects increasingly predominate, leading to the emergence of a 'twin-peaked' pattern.

Besides velocity distribution, turbulence properties and normalized Reynolds stress of jet in waves are also shown and compared with those in stagnant environments in Fig. 20. It is observed that the turbulence profile width expands and its peak values increase when the jet is injected under waves, which is consistent with the findings in the literature [62,63].

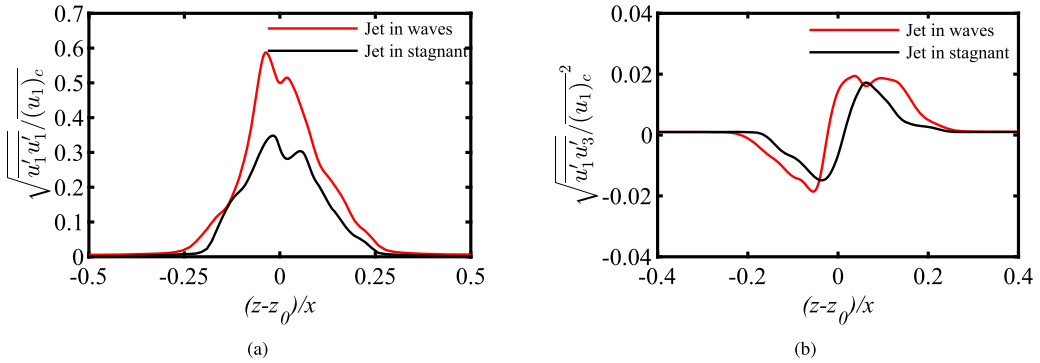

Fig. 20. Comparison of the distribution of (a) axial turbulence intensity; (b) normalized Reynolds stress between jet in stagnant and jet in waves.

Fig. 21 shows the comparison of the vortex identification between jet in stagnant and jet in waves at four different wave phases. Significant differences can be observed in the vortical structures of jet under waves at various wave phases. Notably, small vortical structures are present near the jet orifice, differing markedly from those observed in a stagnant environment. Furthermore, these vortical structures expand significantly when the jet interacts with waves, suggesting enhanced water entrainment into the jet body, a phenomenon attributed to the wave tractive mechanism [64]. Overall, the present developed non-hydrostatic model can well predict the flow pattern of the jet in waves.

5. Conclusion

This paper presents a double-layer σ coordinate non-hydrostatic model to simulate problems related to the free surface for wave-structure/jet interaction. To track the free surface, a Lagrangian-Eulerian method is employed, differing from the approach typically used in most non-hydrostatic models. The applicability of this model has been validated against seven different cases.

First, this model is used to simulate the wave mechanics, including solitary and regular waves propagating at a constant depth. Both the free surface and flow fields demonstrated good agreement with analytical solutions. In addition, a detailed convergence study and the height ratio between the two layers are discussed. Subsequently, the model is applied to the propagation of solitary and regular wave interactions with submerged structures, yielding results that closely align with experimental measurement. This suggests the model's applicability in wave-structure interaction studies. When comparing with single-layer σ coordinate, the surface of submerged obstacles would not move upwards or downwards in response to changes in the free surface when adopting double-layer σ coordinate. Finally, the model is used to simulate the horizontal jet in both stagnant and wave environments. The jet's outflow velocity boundary is generated using the Synthetic-Eddy-Method (SEM) and it is shown that the jet centerline velocity decay and turbulence intensity in stagnant conditions are in good agreement with experimental results. When it comes to the jet in wave environments, the model accurately captured the flow field for fixed orifice location, with observed turbulence intensities exceeding those in stagnant conditions, which is consistent with previous research findings.

The newly developed model demonstrates great promise as a numerical tool for simulating wave-related issues and in engineering design applications. However, it is constrained by the need for sufficient fine grid resolution near the free surface to prevent amplitude and phase errors, which could lead to increased computational costs. In the future, kinetic bottom boundary conditions and time-dependent layer thicknesses will be implemented into the model to simulate more complex problems, such as moving submerged structures. Additionally, the model will incorporate a particle-based approach to simulate sediment transport and deposition processes in coastal dynamics.

CRediT authorship contribution statement

Yuhang Chen: Writing – original draft, Visualization, Validation, Software, Methodology, Investigation, Formal analysis, Data curation. **Yongping Chen:** Writing – review & editing, Supervision, Software, Project administration, Methodology, Investigation, Funding acquisition, Conceptualization. **Zhenshan Xu:** Writing – review & editing, Supervision, Resources, Investigation. **Pengzhi Lin:** Writing – review & editing, Software, Investigation, Formal analysis. **Zhihua Xie:** Writing – review & editing, Validation, Supervision, Investigation, Funding acquisition, Formal analysis, Conceptualization.

Declaration of competing interest

The authors declare that they have no known competing financial interests or personal relationships that could have appeared to influence the work reported in this paper.

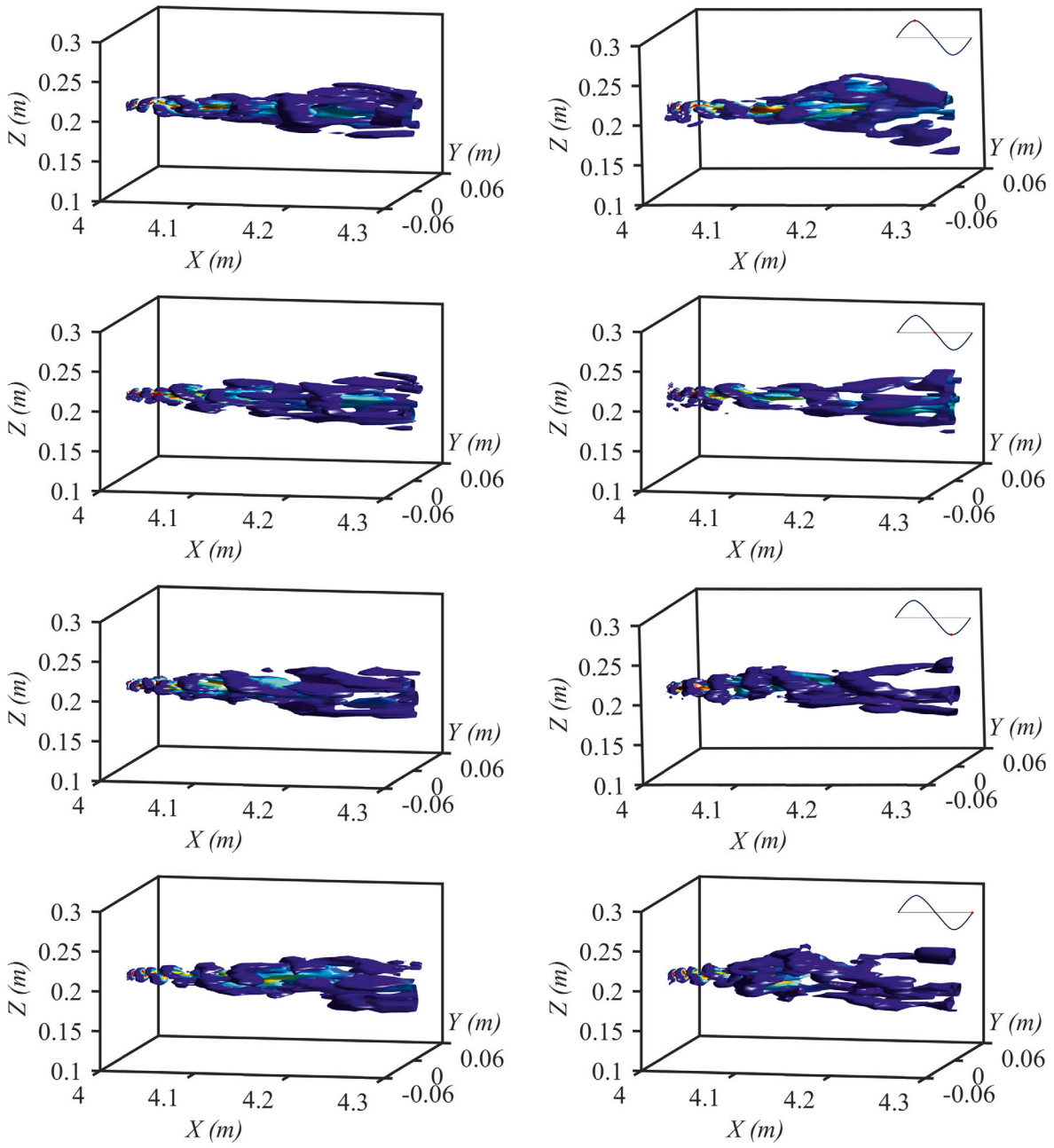

(a) jet in stagnant (b) jet in waves

Fig. 21. Comparison of the vortex identification between (a) jet in stagnant and (b) jet in waves at four different wave phases (from wave peak through wave down-crossing, to the wave trough and finally to the wave up-crossing phases, sequentially showed in vertical lines). The vortical structures are flooded by the axial velocity (blue (0 m/s) to red (0.85 m/s)).

Acknowledgements

Constructive comments from anonymous reviewers have helped to improve the manuscript and these are gratefully acknowledged. This work was supported by the National Key Research and Development Program of China (2023YFC3008100) and the National Natural Science Foundation of China (51979076, 52211530103). The first author is grateful for financial support from the program of China Scholarship Council (202206710100) to work at Cardiff University. Special thanks are also given to Prof. Shunqi Pan and Mr. Baoming Guo for their technical support and encouragement at Cardiff University. ZX is partially supported by the United Kingdom Engineering and Physical Sciences Research Council (EPSRC) grant (EP/V040235/1) and the Alexander von Humboldt Research Fellowship in Germany.

Data availability

Data will be made available on request.

References

[1] B. Zhou, D. Ning, B. Teng, W. Bai, Numerical investigation of wave radiation by a vertical cylinder using a fully nonlinear HOBEM, Ocean Eng. 70 (2013) 1–13.
[2] C. Wang, G. Wu, Interactions between fully nonlinear water waves and cylinder arrays in a wave tank, Ocean Eng. 37 (2010) 400–417.
[3] W. Koo, M. Kim, Fully nonlinear wave-body interactions with surface-piercing bodies, Ocean Eng. 34 (2007) 1000–1012.
[4] M. Christou, C. Swan, O. Gudmestad, The interaction of surface water waves with submerged breakwaters, Coast. Eng. 55 (2008) 945–958.
[5] F. Dias, A.I. Dyachenko, V.E. Zakharov, Theory of weakly damped free-surface flows: a new formulation based on potential flow solutions, Phys. Lett. A 372 (2008) 1297–1302.
[6] C.H. Wu, H. Yuan, Efficient non-hydrostatic modelling of surface waves interacting with structures, Appl. Math. Model. 31 (2007) 687–699.
[7] A.F. Shchepetkin, J.C. McWilliams, The regional oceanic modeling system (ROMS): a split-explicit, free-surface, topography-following-coordinate oceanic model, Ocean Model. 9 (2005) 347–404.
[8] G.S. Stelling, On the Construction of Computational Methods for Shallow Water Flow Problems, Rijkswaterstaat Communications, vol. 35, Government Printing Office, The Hague, the Netherlands, 1983.
[9] M. Zijlema, G. Stelling, P. Smit, Swash: an operational public domain code for simulating wave fields and rapidly varied flows in coastal waters, Coast. Eng. 58 (2011) 992–1012.
[10] S. Beji, K. Nadaoka, A formal derivation and numerical modelling of the improved Boussinesq equations for varying depth, Ocean Eng. 23 (1996) 691–704.
[11] Y.S. Li, S.X. Liu, Y.X. Yu, G.Z. Lai, Numerical modeling of Boussinesq equations by finite element method, Coast. Eng. 37 (1999) 97–122.
[12] M. Tonelli, M. Petti, Hybrid finite volume–finite difference scheme for 2dh improved Boussinesq equations, Coast. Eng. 56 (2009) 609–620.
[13] S. Agarwal, V. Sriram, P.-F. Liu, K. Murali, Waves in waterways generated by moving pressure field in Boussinesq equations using unstructured finite element model, Ocean Eng. 262 (2022) 112202.
[14] M. Ricchiuto, A.G. Filippini, Upwind residual discretization of enhanced Boussinesq equations for wave propagation over complex bathymetries, J. Comput. Phys. 271 (2014) 306–341.
[15] B. Johns, R. Jefferson, The numerical modeling of surface wave propagation in the surf zone, J. Phys. Oceanogr. 10 (1980) 1061–1069.
[16] V. Casulli, R.T. Cheng, Semi-implicit finite difference methods for three-dimensional shallow water flow, Int. J. Numer. Methods Fluids 15 (1992) 629–648.
[17] C.W. Li, T. Yu, Numerical investigation of turbulent shallow recirculating flows by a quasi-three-dimensional $k-\epsilon$ model, Int. J. Numer. Methods Fluids 23 (1996) 485–501.
[18] F.H. Harlow, J.E. Welch, Numerical calculation of time-dependent viscous incompressible flow of fluid with free surface, Phys. Fluids 8 (1965) 2182–2189.
[19] C.W. Hirt, B.D. Nichols, Volume of fluid (VOF) method for the dynamics of free boundaries, J. Comput. Phys. 39 (1981) 201–225.
[20] M. Sussman, P. Smereka, S. Osher, A level set approach for computing solutions to incompressible two-phase flow, J. Comput. Phys. 114 (1994) 146–159.
[21] P. Hergibo, T.N. Phillips, Z. Xie, A moment-of-fluid method for resolving filamentary structures using a symmetric multi-material approach, J. Comput. Phys. 491 (2023) 112401.
[22] C. Ai, Y. Ma, C. Yuan, G. Dong, A 3d non-hydrostatic model for wave interactions with structures using immersed boundary method, Comput. Fluids 186 (2019) 24–37.
[23] P. Lin, L. Cheng, D. Liu, A two-phase flow model for wave–structure interaction using a virtual boundary force method, Comput. Fluids 129 (2016) 101–110.
[24] Z. Xie, T. Stoesser, A three-dimensional Cartesian cut-cell/volume-of-fluid method for two-phase flows with moving bodies, J. Comput. Phys. 416 (2020) 109536.
[25] A. Christou, T. Stoesser, Z. Xie, A large-eddy-simulation-based numerical wave tank for three-dimensional wave-structure interaction, Comput. Fluids 231 (2021) 105179.
[26] G. Stelling, M. Zijlema, An accurate and efficient finite-difference algorithm for non-hydrostatic free-surface flow with application to wave propagation, Int. J. Numer. Methods Fluids 43 (2003) 1–23.
[27] M. Zijlema, G.S. Stelling, Further experiences with computing non-hydrostatic free-surface flows involving water waves, Int. J. Numer. Methods Fluids 48 (2005) 169–197.
[28] M. Zijlema, G. Stelling, Efficient computation of surf zone waves using the nonlinear shallow water equations with non-hydrostatic pressure, Coast. Eng. 55 (2008) 780–790.
[29] G. Ma, F. Shi, J.T. Kirby, Shock-capturing non-hydrostatic model for fully dispersive surface wave processes, Ocean Model. 43 (2012) 22–35.
[30] P. Lin, C.W. Li, A σ-coordinate three-dimensional numerical model for surface wave propagation, Int. J. Numer. Methods Fluids 38 (2002) 1045–1068.
[31] P. Stansby, J. Zhou, Shallow-water flow solver with non-hydrostatic pressure: 2d vertical plane problems, Int. J. Numer. Methods Fluids 28 (1998) 541–563.
[32] Y. Chen, C. Li, C. Zhang, Large eddy simulation of vertical jet impingement with a free surface, J. Hydrodyn. 18 (2006) 148–155.
[33] Z. Xu, Y. Chen, J. Tao, Y. Pan, C. Zhang, C. Li, Modelling of a non-buoyant vertical jet in waves and currents, J. Hydrodyn., Ser. B 28 (2016) 778–793.
[34] C.W. Li, B. Zhu, A sigma coordinate 3d k–ϵ model for turbulent free surface flow over a submerged structure, Appl. Math. Model. 26 (2002) 1139–1150.
[35] P. Lin, A multiple-layer σ-coordinate model for simulation of wave–structure interaction, Comput. Fluids 35 (2006) 147–167.
[36] C. Ai, S. Jin, B. Lv, A new fully non-hydrostatic 3d free surface flow model for water wave motions, Int. J. Numer. Methods Fluids 66 (2011) 1354–1370.
[37] G. Ma, A.A. Farahani, J.T. Kirby, F. Shi, Modeling wave-structure interactions by an immersed boundary method in a σ-coordinate model, Ocean Eng. 125 (2016) 238–247.
[38] A. Kang, P. Lin, Y.J. Lee, B. Zhu, Numerical simulation of wave interaction with vertical circular cylinders of different submergences using immersed boundary method, Comput. Fluids 106 (2015) 41–53.
[39] J. Smagorinsky, General circulation experiments with the primitive equations: I. The basic experiment, Mon. Weather Rev. 91 (1963) 99–164.
[40] P. Lin, P.L.F. Liu, A numerical study of breaking waves in the surf zone, J. Fluid Mech. 359 (1998) 239–264.
[41] J.C. Park, M.H. Kim, H. Miyata, Fully non-linear free-surface simulations by a 3d viscous numerical wave tank, Int. J. Numer. Methods Fluids 29 (1999) 685–703.
[42] N. Jarrin, S. Benhamadouche, D. Laurence, R. Prosser, A synthetic-eddy-method for generating inflow conditions for large-eddy simulations, Int. J. Heat Fluid Flow 27 (2006) 585–593.
[43] J. Lu, H. Dai, Large eddy simulation of flow and mass exchange in an embayment with or without vegetation, Appl. Math. Model. 40 (2016) 7751–7767.
[44] H. Schlichting, J. Kestin, Boundary Layer Theory, vol. 121, Springer, 1961.
[45] Z. Lu, M. Yuan, The LDA measurement of turbulent flow in square duct and the comparison of some flow characteristics with pipe flow, Acta Mech. Sin. 18 (1986).
[46] X. Wu, P. Moin, A direct numerical simulation study on the mean velocity characteristics in turbulent pipe flow, J. Fluid Mech. 608 (2008) 81–112.
[47] N.N. Janenko, The Method of Fractional Steps, vol. 160, Springer, 1971.
[48] C.W. Li, Advection-dispersion simulation by minimization characteristics and alternate direction-explicit methods, Appl. Math. Model. 15 (1991) 616–623.
[49] L. Zhu, C.W. Li, Error study on numerical approximation of radiation boundary condition for one-dimensional wave equation, Commun. Numer. Methods Eng. 9 (1993) 475–482.

[50] J.-J. Lee, J.E. Skjelbreia, F. Raichlen, Measurement of velocities in solitary waves, J. Waterw. Port Coast. Ocean Div. 108 (1982) 200–218.
[51] P. Lin, Numerical Modeling of Water Waves, CRC Press, 2008.
[52] J.J. Stoker, Water Waves: The Mathematical Theory with Applications, vol. 36, John Wiley & Sons, 1992.
[53] F. Zhuang, J.-J. Lee, A viscous rotational model for wave overtopping over marine structure, in: Proc 25th Int Conf Coastal Eng. ASCE, 1996, pp. 2178–2191.
[54] J. Dong, L. Xue, K. Cheng, J. Shi, C. Zhang, An experimental investigation of wave forces on a submerged horizontal plate over a simple slope, J. Mar. Sci. Eng. 8 (2020) 507.
[55] Y. Chen, C.W. Li, C. Zhang, Numerical modeling of a round jet discharged into random waves, Ocean Eng. 35 (2008) 77–89.
[56] S. Beji, J. Battjes, Experimental investigation of wave propagation over a bar, Coast. Eng. 19 (1993) 151–162.
[57] H. Yuan, C.H. Wu, A two-dimensional vertical non-hydrostatic σ model with an implicit method for free-surface flows, Int. J. Numer. Methods Fluids 44 (2004) 811–835.
[58] Y. Chen, P. Sun, Y. Wang, Z. Xu, D. Jiang, Y. Zhang, Effects of discharge angles on hydrodynamics and dilution of round jets in wave environment, Adv. Water Sci. 28 (2017) 898–907.
[59] S.J. Kwon, I.W. Seo, Reynolds number effects on the behavior of a non-buoyant round jet, Exp. Fluids 38 (2005) 801–812.
[60] H.J. Hussein, S.P. Capp, W.K. George, Velocity measurements in a high-Reynolds-number, momentum-conserving, axisymmetric, turbulent jet, J. Fluid Mech. 258 (1994) 31–75.
[61] C. Bogey, C. Bailly, Turbulence and energy budget in a self-preserving round jet: direct evaluation using large eddy simulation, J. Fluid Mech. 627 (2009) 129–160.
[62] R. Koole, C. Swan, Measurements of a 2-d non-buoyant jet in a wave environment, Coast. Eng. 24 (1994) 151–169.
[63] S.C. Hsiao, T.W. Hsu, J.F. Lin, K.A. Chang, Mean and turbulence properties of a neutrally buoyant round jet in a wave environment, J. Waterw. Port Coast. Ocean Eng. 137 (2011) 109–122.
[64] J.-M. Chyan, H.-H. Hwung, On the interaction of a turbulent jet with waves, J. Hydraul. Res. 31 (1993) 791–810.